We are IntechOpen,
the world's leading publisher of
Open Access books
Built by scientists, for scientists

3,900
Open access books available

116,000
International authors and editors

120M
Downloads

Our authors are among the

154
Countries delivered to

TOP 1%
most cited scientists

12.2%
Contributors from top 500 universities

BOOK CITATION INDEX
CLARIVATE ANALYTICS
INDEXED

WEB OF SCIENCE™

Selection of our books indexed in the Book Citation Index
in Web of Science™ Core Collection (BKCI)

Interested in publishing with us?
Contact book.department@intechopen.com

The New Youth of the *In Situ* Transmission Electron Microscopy

Alberto Casu, Elisa Sogne, Alessandro Genovese,
Cristiano Di Benedetto, Sergio Lentijo Mozo,
Efisio Zuddas, Francesca Pagliari and Andrea Falqui

Additional information is available at the end of the chapter

Abstract

The idea of *in situ* transmission electron microscopy (TEM) and its possible ramifications were proposed at the very dawn of electron microscopy, but the translation from theory to practice encountered many technological setbacks, which hindered the feasibility of the most elaborated approaches until recent times. However, the several technological improvements achieved in the last 10–15 years filled this gap, allowing the direct observation of the dynamic response of materials to external stimuli under a vast range of conditions going from vacuum to gaseous or liquid environment. This resulted in a blossoming of the *in situ* TEM and scanning TEM (STEM) techniques to a new youth for a vast, growing range of applications, which cannot be rightfully detailed in a short span; therefore, this chapter should be intended as a guide highlighting a selection of the most inspiring, recently achieved results.

Keywords: analytical electron microscopy, environmental transmission electron microscopy, *in situ* transmission electron microscopy, scanning transmission electron microscopy, transmission electron microscopy

1. Introduction

The idiom "seeing is believing" is very old and has been often used since its religious inception to the present day as the title of novels, songs, movies, and documentaries. However, it is also the actual utterance of any *in situ* microscopist. So, what is the *in situ* transmission electron microscopy (TEM)? It consists in the ability to look by TEM and in real time at the dynam-

ic behavior of a material as a consequence of an external *stimulus*, so providing an insight into its properties and modifications while they are happening. This kind of information is inaccessible by other techniques at the atomic scale, which is used to perform imaging, structural and/or compositional analyses by TEM. The main difference with respect to any other TEM observation technique lies in the fact that instead of carrying out experiments on specimens outside the microscope and using the TEM for observations before and after the experiments' completion, the *in situ* TEM permits to image the evolution of materials while it is occurring, thus not losing any information about intermediate states. As briefly mentioned above, the evolution over time of samples under TEM observation takes place under an external *stimulus*. Then, it is possible changing the environment around the TEM sample in several ways: varying the temperature up to very high or down to very low values; keeping the specimen in thermally controlled static or dynamic gaseous environment, in the latter case also controlling the gas pressure; putting the sample in different liquids under static or flowing regime, also to perform local chemical/electrochemical reactions; applying to it local strain, compression, nanoindentation; and putting it in an electrical or magnetic field, as well as irradiating it by electrons or light.

Why we titled this chapter "The new youth of the *in situ* electron microscopy"? Because if on the one hand the possibility to perform *in situ* experiments was always chased resolutely since the beginning of TEM studies, on the other hand it was just the dramatic advancements achieved by TEM in the last 10–15 years that gave the necessary impulse to further develop the *in situ* studies. First, TEM—even in the scanning mode (STEM)—has recently known a new and strong evolution with respect to the past. The two fundamental events that greatly improved the way to perform (S)TEM imaging consisted in the availability of both ultrabright electron sources [1] and spherical aberration correctors [2, 3] for either the condenser or the objective lens. The first improvement made electron beams very bright allowing to work in both TEM and STEM geometries with very low exposition times for both imaging and spectroscopic acquisition. The second one permitted to achieve unprecedented spatial resolution, down to less than 0.1 nm, using conventional electron acceleration voltages. Furthermore, the last decade also saw other important developments: electron energy resolution was improved to less than 0.1 eV by using beam monochromators [4] or cold field emission electron sources [5], while the most recent silicon drift detectors (SDD) with very large solid angle for energy-dispersive spectroscopy (EDS) [6], electron energy loss spectroscopy (EELS) image filters [7], and the ultrafast CMOS cameras [8] allowed to investigate the specimens' evolution in terms of both imaging and elemental analyses down to the atomic scale with very high time resolution and under very low electron dose conditions, respectively. As a consequence, all the (S)TEM-based analytical and imaging techniques largely benefited from these achievements and also pushed up the capability to realize further *in situ* studies mainly by means of novel and dedicated microscopes or specimen holders, which actually work as small "laboratories" providing the means to submit the samples to all the possible external *stimuli* mentioned above. In most of the cases, micro- and nanoelectromechanical systems (MEMS and NEMS, respectively) as well as nanodevices led to the miniaturization of the specimen holders' or stages' components. This allowed performing *in situ* experiments with exceptional minimization of the sample drift, currently reduced to about 1 nm min^{-1} and

characterized by an increase in complexity and number of possible *stimuli*, while granting a fine devices' control and the simultaneous recording of massive amounts of data.

Due to the current and continuously growing vastness of the *in situ* (S)TEM field, this chapter shows only some of the most recent and exciting innovations and results achieved in this field. Not all applications are then represented here, but we decided to focus the attention mainly on the *in situ* (S)TEM techniques and experiments that in our opinion well represent the most important, recently achieved novelties with the main aim of showing the improvement in quality of today's scientific results with respect to the past.

The chapter starts with a section dedicated to the *in situ* heating experiments because heating any sample upon the TEM high vacuum conditions is a decades-old kind of experiment that was affected by two concomitant limitations until few years ago. Since the heating was usually realized by a small furnace surrounding the sample, the first unavoidable limitation was due to the thermal dilatation of the metal constituting the TEM grid during all thermal ramps as a consequence of a huge drift suffered by the whole sample that made recording any image or analytical data impossible until the thermal steady state was reached. The second effect was less crucial and due to the high amount of heat produced by the furnace: the increase in temperature was unavoidably accompanied by the emission of highly intense infrared (IR) radiation coming from the heated furnace and TEM grid. This IR emission saturated any EDS detector even at low temperature (i.e., less than 100°C), making impossible to use this spectroscopic technique to qualitatively or quantitatively analyze the elements constituting the samples. However, thanks to the new MEMS-based heating holders, where a heating chip has substituted the furnace that heated the TEM grid, both these limitations have been dramatically reduced. First, it is now possible reaching sample drift as low as 1 nm min^{-1} during the thermal ramps. Second, being the heating element much smaller than the classical furnace, the power needed to reach high temperatures is also much lower than the one needed to increase the temperature of a standard metal TEM grid, resulting in a strong limitation of the produced heat. This in turn allows the use of EDS for analyzing samples with temperatures up to some hundreds of degrees without saturating the EDS detector. In the following section, the attention is then focused on a sort of "variation on a theme" of the *in situ* sample heating. In this case, a different sample environment is taken into account, being it a gaseous one developed to study *in situ* solid-gas reactions. This section explains the two main current routes to perform this kind of experiments, namely, (a) by using a very small and physically isolated volume where the gas could either be sealed or let flow inside the TEM sample holder; (b) by inserting a heating sample holder in a particular kind of microscope, usually known as environmental TEM (E-TEM), featuring a portion of the TEM column filled with gas at a controlled pressure and limited by two zones where a differential pumping system prevents any gas leak in the rest of the TEM column and gun. Section 3 of this chapter is dedicated to a sort of further development of the gas-solid *in situ* (S)TEM techniques and devices shown in the previous section, with the aim to realize *in situ* imaging of samples immersed in a liquid environment and to follow real-time chemical reactions that are occurring in a liquid solution. From a historical point of view, these kinds of experiments had already been attempted just after the TEM invention, between the end of the 1930s and the beginning of the 1940s of the

twentieth century, but they became effectively attainable just in very recent years. In this regard, the most interesting aspects of performing *in situ* liquid (S)TEM experiments consist in the fact that, first, this is the only TEM technique that allows the observation of living cells, although with some limitations that are discussed below and, second, that the high electron scattering power of any liquid requires slightly different sample configurations and preparations, depending on the geometry (TEM or STEM) that is used to perform the *in situ* imaging.

2. *In situ* heating TEM experiments in vacuum

Studies involving temperature and its effects on the features and evolution of various systems are most common in a very broad number of different branches, ranging from fundamental research and going to strictly applicative performance issues. Despite the very different focus, all these kind of studies rely on the basic assumption that the goodness and reliability of the results will necessarily go through trying to obtain the most thorough description of the evolution of the system and of the phenomena leading to said evolution. Thus, while TEM stands as the obvious choice for gathering a vast array of accurate direct structural information, the choice of performing *in situ* rather than *ex situ* heating treatment lies in the possibility of obtaining as precise data as possible, thus limiting the temperature ranges where unnoticed transient variations could take place. The *ex situ* approach consists in an out-of-TEM-column annealing and in the subsequent observation by TEM of its results, so it is a simpler setup from the point of view of the actual TEM (only an external furnace/heating source is required), which does not affect the microscope's performance in terms of spatial resolution. Conversely, this approach is inherently limited by the fact that the study of a temperature-dependent system would require the *ex post* reconstruction of the intermediate states by repeating the annealing at different user-defined temperatures. Leaving aside any consideration regarding the samples, this approach in principle allows for a very precise control over temperature, but also retains a degree of uncertainty over the evolution of the system given by the user-defined rate of temperature sampling, which must obviously be a discrete, not continuous, one.

On the other hand, the *in situ* approach implies that the annealing takes place inside the TEM column by using a dedicated heating holder, thus allowing a direct, continuous observation of the temperature-dependent evolution of the sample. The *in situ* approach to annealing seems the most promising one, but in practice it relies heavily on the technological/technical advancements in both design and performance of the heating holders, namely, minimizing the thermal mechanical drift associated with the heating of the holder and extending its temperature range while improving the precision of temperature control and thermal stability of the holder, thus allowing the possibility to run better controlled and more elaborated experiments.

In this framework, the evolution observed in the design of heating holders, going from homemade custom ones [9, 10] to commercial furnace-type ones [11, 12] to the most recent developments involving strongly localized micron-wide heating areas, affected the feasibility of heating experiments.

In furnace-type heating holders, the annealing is achieved by heating a section located at the tip of the TEM holder, where the TEM grid is lodged and clamped. A heating filament in
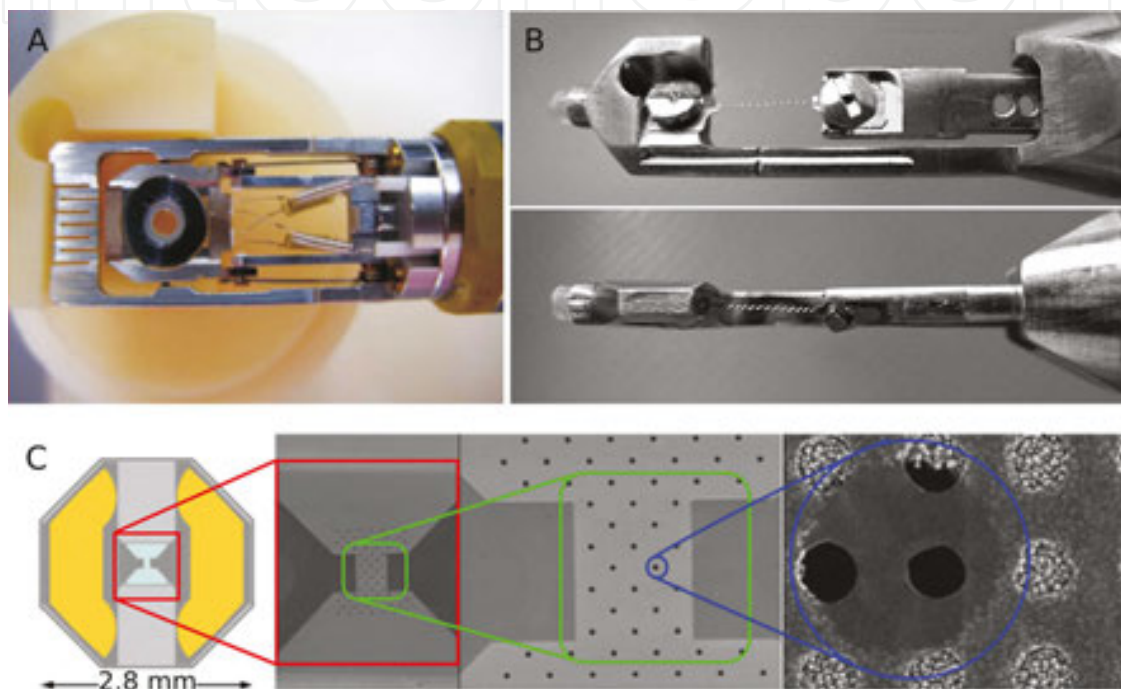
proximity to the TEM grid is responsible for the heating of this "hot zone," while the temper-ature can be measured by a thermocouple or a temperature-to-current calibration curve (**Figure 1A**).

Obviously, the hot region of the furnace must be mechanically stable within the working temperature range in order to minimize the mechanical drift associated with the thermal expansion of the furnace, while being as thermally isolated as possible from the rest of the holder in order to limit the heat conduction to the rest of the tip/holder and the consequent instability in reaching and measuring the correct temperature. Thus, the improvement of this category of holders goes through finding appropriate materials for the different components of the tip and designing a heating system that maximizes both the heating performance and the thermal and mechanical stabilities while minimizing the undesired side effects, such as heat dissipation to the rest of the holder and high power consumption.

From the materials point of view, this implies lowering the coefficient of thermal expansion for the ones used in the furnace, while those used to connect the furnace to the tip must also guarantee low thermal conductivity, since the connections should insulate the furnace against the heat conduction to the holder. Moreover, the rest of the tip should have high heat capacity in order to minimize the heating by irradiation coming from the furnace, thus keeping the holder as close as possible to room temperature. The results achieved with regard to the materials must be supported by improving the design of the holder in order to increase its ease of use and its efficiency in terms of performance vs. power consumption. This means, for example, trying to minimize the size of the furnace (and consequently increasing the available heating rates while decreasing the power consumption necessary for any heat treatment) or designing tips that decrease the heat dispersion from the furnace. However, one inherent problem of indirect-heating holders, such as the furnace-based ones, lies in the gradient of temperature occurring between the heating furnace and the TEM grid during the annealing: this difference can be minimized in stable temperature conditions, but it still induces a transient state of thermal imbalance and mechanical drift due to thermal expansion.

In this framework, the run for improving the performance of heating holders leads to the introduction of different solutions that abandoned the furnace-based architecture for anneal-ing TEM samples (**Figure 1B** and **C**). Kamino holders [13] adopted heating wires as a direct source of Joule heating and as a support for the TEM sample: this architecture allows for a direct heating of the sample and higher annealing temperatures but lacks versatility, because samples need to be supportable by the heating wire. A further step in this direction is repre-sented by heating holders based on MEMS (microelectromechanical systems) chips technology [14, 15]. These chips are constituted by a semiconductor (usually Si or Si-based material) as main body, overlaid by a thin film and featuring a small, electron-transparent area devoted to the heating and subsequent TEM analysis, thus effectively combining the heating element and the TEM grid in the same object. The presence of a support film allows for greater versatility in terms of possible samples, while dedicated conductive wirings provide the heating and temperature measurements of the heating area in a fashion similar to the furnace-type holders: a heating wire acts as an electrical furnace, while a second one is used as a temperature probe against a resistance-to-temperature calibration curve. Given the small dimensions of the

heating area (usually less than 0.1 mm² wide) with respect to those of the whole chip, choosing a material with high thermal conductivity enables the chip itself to act both as a thermal sink with respect to the heating area and as an insulating buffer with respect to the holder. On the other hand, the engineering of a miniaturized heating area with low heat capacity implies using smaller heating currents. The combination of these characteristics allows faster temperature ramps and faster cooling rates by the sole variations in heating current values, resulting in a more precise control over the desired temperatures and an overall expansion of the possibilities of annealing experiments.

Figure 1. (A) Top view of a furnace-based heating holder. The circular hole at the center of the furnace serves as lodging for the TEM grid. Adapted with permission from [116]; (B) top and side views of a Kamino-type, direct-heating holder displaying a fine tungsten wire heater. Adapted with permission from [117]; (C) top view schematic of MEMS-based heater chip. Backscattered and secondary electron images of the central region of the chip at increasing magnification reveal the structure of its core and the carbon-film-covered holes. Adapted with permission from [15].

Considering these innovations in the more general framework of the recent achievements of TEM, the possibility of performing *in situ* annealing experiments with atomic resolution has become a realistic goal, shedding new light on the fine mechanisms of already well-established areas of interest and on previously impossible experimental routes.
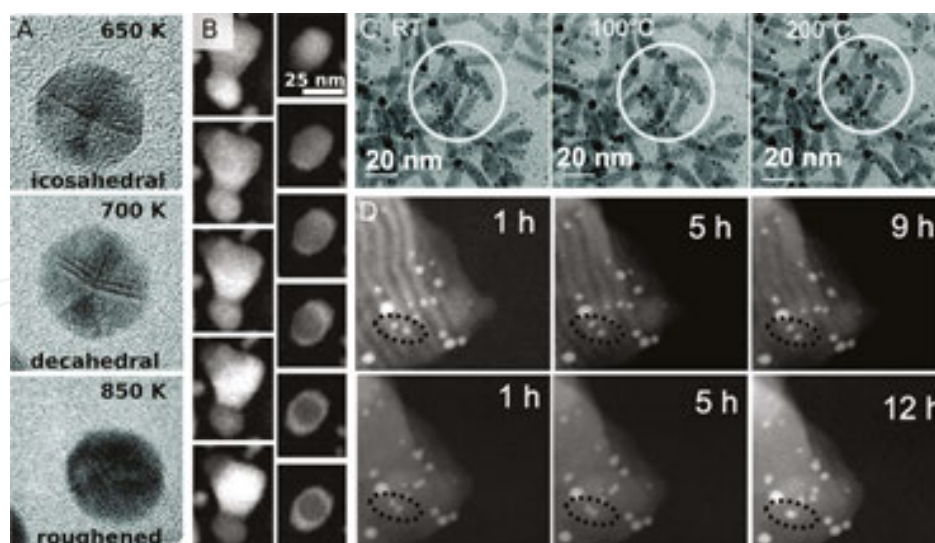
2.1. *In situ* TEM heating in Au nanoparticles

The study of colloidal metallic nanoparticles (NPs) has been a major research subject during the past decades, at first to show, then to study and modify their properties for a vast array of possible applications, such as biomedical, sensor technologies, energy storage and nanocatalysis. The development and improvement of imaging techniques such as TEM allowed a clearer comprehension on the connections between structural characteristics and physical

properties at the nanoscale, which are required to understand and optimize their use in diverse applications.

In this general context, Au NPs were a constant object of interest in studies describing different synthetic methods and morphologies, their properties, and their possible applications [16–20]. However, regardless of the particular field of application, any engineering attempt would benefit from a detailed analysis of the morphological and structural transformations happening at the nanoscale. This is the reason for developing and improving a nanoscale phase diagram for Au NPs, i.e., a predictive map of their structural-, morphology-, and temperature-dependent stable configurations. Previous experimental and theoretical studies on nanogold [21, 22] were recently improved thanks to *in situ* annealing studies, taking advantage of the improved temperature control granted by MEMS-based technology and leading from qualitative to quantitative phase diagrams. Barnard [23] provided a comparative study between their calculated phase map and *in situ* annealing high resolution TEM (HRTEM) data. The quantitative phase map was obtained by combining the calculated free energy of different motifs according to a free energy vs. temperature vs. size model and illustrated the stable motifs for gold NPs, while the annealing experiments (up to 1000 K) provided the phase evolution data for NPs of different sizes, showing the temperature-driven evolution from ichosaedral, to decahedral, and finally to a disordered motif with "roughened" surface (**Figure 2A**). These results were further validated and refined by devoting attention to the high temperature regime and surface roughening [24]. In fact, *in situ* HRTEM annealing data showed that despite a modest size variation at lower temperatures, a consistent decrease in size could be observed once the thermal threshold of surface roughening had been exceeded. This experimental trend was consistent with previous theoretical models, but also highlighted which physical phenomena took place in the premelting regime. The occurrence of NPs with an amorphous, irregular surface and a crystalline core excluded an amorphization by melting the whole NP in favor of a coexisting liquid/solid state, where the evaporation of the liquid molten phase is responsible for the size variation.

The relationship between theoretical and experimental data with regard not only to the structural evolution of the NPs but also to their so-called roughened and melting states proved the suitability of this course of action for obtaining a full structural characterization. In fact, a similar approach was recently tried by Baumgardner [25], who studied the structural evolution of a heterogeneous Au:Fe$_2$O$_3$ NP system at elevated temperatures by *in situ* annealing. In particular, by taking advantage of Z-contrast in high angle annular dark-field scanning TEM (HAADF-STEM), it was possible to follow the evolution from a dual population of Au and Fe$_2$O$_3$ NPs to the formation of new mixed Au/Fe$_2$O$_3$ NPs via fluid shape transformation. Two possible morphologies emerged, namely, phase-segregated Fe$_2$O$_3$/Au structures or surface-alloyed NPs with an Au/Fe layer in between the iron oxide core and the gold shell. The evolution of phase-segregated and surface-alloyed NPs was further monitored by increasing the *in situ* annealing temperature while collecting HAADF-STEM and chemical data (**Figure 2B**). Thus, variations in chemical composition and size of each NP vs. temperature were combined as a nanosized phase diagram, which works as a compositional stability phase map for this binary system.

Figure 2. (A) Representative HRTEM images showing the phase variations of a 7.5 nm wide Au NP as a function of temperature. Adapted with permission from [23]; (B) phase transition from alloy to phase segregated (left) or core/ shell nanoparticles (right). Adapted with permission from [25]; (C) HRTEM images showing the evolution of Au@CdSe networks during the *in situ* annealing experiment. Adapted with permission from [27]; (D) HAADF-STEM images showing the motion of Au NPs in SBA-15 during *in situ* TEM heating experiments conducted at 550°C (top) and 700°C (down). Adapted with permission from [28].

On the other hand, *in situ* annealing TEM is also a valuable tool for less systematic and more application-based studies, focused on trying to take into account (and possibly take advantage of) the properties of Au NPs for developing nanosized heterostructures for different applications. In this regard, a good example is given by the mobility and sintering of Au NPs. The mobility was a key factor in studying CdSe nanorods (NRs) decorated with Au domains and their structural and morphological evolution under thermal annealing for possible applications in the fields of electronics and photovoltaics [26, 27]. While at room temperature the Au decoration of CdSe NRs consisted in small Au NPs attached to the lateral facets of the rods and larger Au NPs located at their tips, heating the samples above 200°C caused the migration of the small NPs toward the tips and the subsequent ripening of the larger Au NPs. In particular, the ripening of Au NPs at the tips of nearby CdSe rods led to bigger sized NP/NR interfaces, effectively forming a robust network (**Figure 2C**). Further investigations on the charge transport mechanisms showed that the annealing improved the conductance of these networks, thus making them viable candidates in the development of bottom-up electronic devices.

Conversely, the mobility and sintering of Au NPs is a drawback in the case of catalysis, where stability problems caused by deactivation due to NP sintering at high temperatures are well-known problems for metallic NP-based catalysts. Thus, a deeper comprehension of the sintering mechanism of NPs inside a porous matrix is a basic research study with immediate applicative repercussions. Liu et al. [28] studied the migration of Au NPs inside the ordered channels of mesoporous silica via *in situ* TEM annealing (**Figure 2D**). By comparing the migration of Au NPs inside silica mesoporous matrices with different pore diameters and micropore volumes at high temperatures, they observed that in fact the sintering was sub-

stantially suppressed by the largest silica matrix with largest micropore volumes, since the Au NPs tend to be embedded in the micropores of the mesochannel walls. This result highlighted the main importance of abundance and size of micropores to hinder the migration and sintering of the NPs. Moreover, by performing *in situ* STEM-EELS during the annealing and observing the local variations in the plasmonic features of a region with two coalescing NPs, they could suggest that an expansion of the conduction electron clouds induced by the annealing could trigger electron-tunneling-induced coalescence of nearby Au NPs.

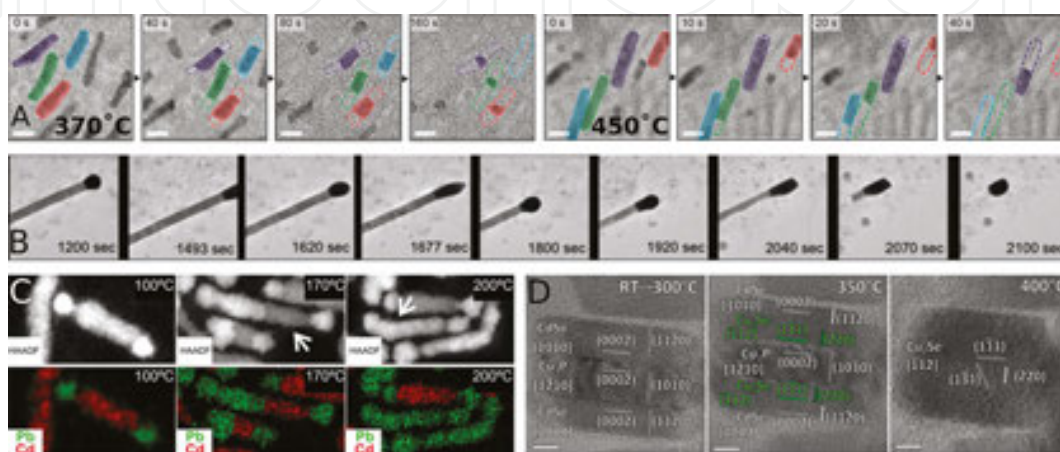## 2.2. *In situ* chemical reactions of semiconductor-based materials

Semiconductors represent another broad research subject in the fields of chemistry and material science, but recent studies conducted on these systems offer a different prospective on the role and possibilities of *in situ* annealing experiments.

In fact, while colloidal synthesis is a well-known route to synthesize and fine-tune NPs with well-defined crystal structure, shape and size [29, 30], *in situ* annealing TEM represents a useful tool not only to investigate (at atomic level and in real time) the properties and stability of promising nanomaterials [31–37] but also to trigger extensive modifications in nano-materials of technological interest.

In this context, the studies by Hellebusch et al. [34] and Hudak et al. [35] represent perfect examples of basic research of immediate applicative interest, since both present stability tests for materials that are already being used as building blocks in a vast range of applications. In particular, Hellebusch et al. [34] investigated the *in situ* sublimation of CdSe NRs in order to understand if the sublimation could influence their facet stability and the possible role of surface ligands. While the sublimation was always anisotropic, a temperature-dependent effect was observed: the mass loss occurred either noncontinuously from both ends of the NRs at lower temperatures or continuously from one end at higher temperatures (**Figure 3A**). In both cases, the NR sublimation and the mass loss occurred along the long *c*-axis, featuring the least stable facets. After reaching a transition state with a particle length of 2–3 nm (without variations in the NR diameter), the sublimation proceeded along *ab*-axes until the full subli-mation was achieved. Also, an explanation to the dual sublimation trend involving surface ligands and generic contaminants was proposed. Taking into account the presence of a superficial layer coating the NRs, it was proposed that the NR sublimation fronts were hindered by this layer and that the sublimation could start whenever one of the tips was "freed" by nucleation or desorption of the contaminant. Thus, similar sublimation and the contaminant deposition rates at lower temperature would imply a noncontinuous sublimation, while at higher temperatures the sublimation could be favored, leading to a continuous sublimation process.

On the other hand, Hudak et al. [35] investigated the dissolution of Au-decorated SnO_2 nanowires. *In situ* TEM annealing experiments were conducted between 400 and 800°C and etching was observed at $T > 450°C$ with Au moving along the wires and consuming them by a solid-liquid-vapor (SLV) dissolution mechanism. In particular, the finer temperature control granted by MEMS-based holders showed that Au motion was indeed a temperature-guided process with the motion/dissolution rate being activated, accelerated, or quenched by reaching,

going beyond, or below the threshold temperature. By studying the evolution of the Au/SnO$_2$ interface against temperature, the SLV mechanism was observed: reaching the threshold temperature activated the diffusion of Sn in the Au tip and the subsequent melting of the Au/Sn alloy to a droplet; the interfacial SnO$_2$ dissolved in the droplet, leading to the supersaturation of Sn and its ejection via evaporation or surface diffusion (**Figure 3B**). Depending on the temperature and the size, the Au/Sn droplet could overcome adhesion to the substrate and move through the NW by the incorporation/ejection of Sn, resulting in a temperature-controlled etching mechanism.

Figure 3. (A) CdSe NRs sublimation during *in situ* annealing experiments at different temperatures. Scale bars are 10 nm. Adapted with permission from [34]; (B) dissolution of the SnO$_2$ nanowire into the Au catalyst tip during *in situ* heating experiments. Field of view is 870 nm. Adapted with permission from [35]; (C) HAADF-STEM images and the corresponding STEM-EDX elemental maps of dumbbell heteronanostructures collected during *in situ* annealing experiments at different temperatures. Adapted with permission from [36]; (D) HRTEM images of a single CdSe/Cu$_3$P/CdSe heterostructure collected during an *in situ* annealing experiment from RT to 400°C, where the sole Cu$_2$Se phase is observed. Scale bars are 5 nm. Adapted with permission from [37].

An alternative approach to *in situ* experiments takes advantage of the annealing to introduce chemical transformations in candidate materials. Yalcin et al. [36] showed the evolution of PbSe-CdSe nanodumbbell heterostructures (HSs) subject to *in situ* evaporation-induced cation exchange (CE) by a solid-solid-vapor (SSV) epitaxial growth mechanism. The annealing-driven Cd evaporation from the superficial sites and the increased mobility of Cd along the HSs triggered the migration of Cd vacancies from the surface to the PbSe/CdSe interface, where they recombined with Pb atoms, forming Pb vacancies. Subsequent recombination with excess Pb adsorbed on the PbSe domains led to the growth of the PbSe phase at the expense of the CdSe phase (**Figure 3C**), leading to the reduction or the complete substitution of the CdSe phase.

Also, De Trizio et al. [37] obtained a new phase through substitution of both cationic and anionic atomic species by performing *in situ* annealing on a "sandwich"- type CdSe/Cu$_3$P/CdSe HS. Structural and chemical analyses highlighted that the exchange reaction was a two-step process with Cu first diffusing and substituting Cd to form Cu$_2$Se in the peripheral regions of the HS (as proven by the blurring of the Cu$_3$P/CdSe interface and the rearranging of CdSe) and

Se subsequently diffusing to the Cu_3P region to finally form a single-phase Cu_2Se NP (**Figure 3D**). Both studies showed ordinate fronts of atomic diffusion and substitution, resulting in the formation of new phases where the orientations of the starting structures are mimicked, while the shape and size of the starting nanostructures are maintained.

Thus, *in situ* TEM annealing represents a solid tool not only to study the stability of a vast array of nanostructures but also to finely tune the parameters leading to their modification.
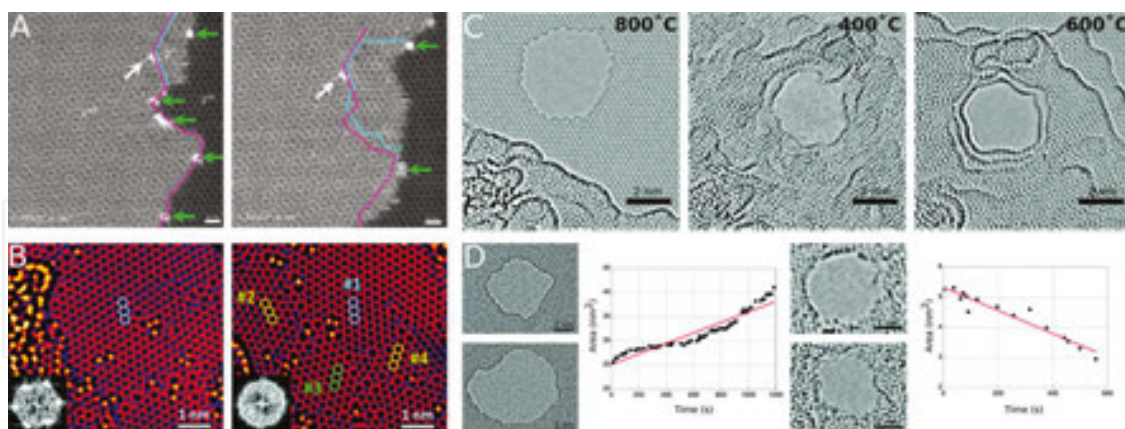
2.3. *In situ* TEM heating for graphene studies

Graphene, with its unique physicochemical properties [38–40], has been the subject of various studies voted to better understand its properties in response to external *stimuli* at the nano- or atomic scale. In this context, the use of *in situ* TEM to investigate the graphene response during annealing processes permits to study and comprehend how its behavior at high temperature can be exploited to tune the growth and engineer its properties for possible applications.

In particular, the control over orientation during the growth of the graphene layer has been an ongoing issue since graphene layers were first produced by mechanical exfoliation of bulk graphite by Gemin and Novoselov in 2004 [41] regardless of the growth technique (CVD [42], thermal decomposition of SiC [43] and molecular beam epitaxy (MBE) [44]), and investigating its growth process is a mandatory prerequisite for a successful application. In this perspective, *in situ* TEM annealing provides the chance to study how the temperature can influence the growth process of graphene. Liu reported, through aberration-corrected STEM analysis, a direct observation of graphene growth and domain boundary formation obtained by annealing bilayer graphene (BLG) and using the hydrocarbon residues from the microscope column as a carbon source for in-plane graphene growth at the step edge of the BLG substrate [45]. By keeping the electron beam energy below a threshold of ~50 kV to prevent knock-on damage in graphene structure [46] and annealing to 700°C, an extra growth was observed from the edge of the second layer of a single BLG-crystal following mechanisms determined by step-edge structures with residual Si atoms from the CVD fabrication process acting as catalysts during the graphene growth and sliding over the graphene edges during e-beam scanning (**Figure 4A**). Moreover, it was possible to investigate the relation between growth rate and residual hydrocarbon gas pressure by changing the vacuum conditions inside the TEM column (in the range 1.0–2.9 ×10^{-5} Pa), thus finding faster growth rates when more residual hydrocarbon gases were left in the TEM column. In fact, the step-edge in-plane growth is a combined mechanism of physical absorption of C atoms and catalytic effect of Si atoms present on bilayer edges, where the thermal treatment provides the needed activation energy and the electron beam accumulating hydrocarbon molecules over the scanned area. Graphene growth is strongly dependent on the equilibrium between the number of available C atoms and the time needed for the C-to-graphene bonding to occur: if the C atoms do not have enough time to bond in an energetically favorite site, then graphene will be just contaminated with amorphous C. In fact, graphene observed in STEM mode at room temperature and low vacuum condition (non-zero pressure of gaseous hydrocarbons) presented contamination by amorphous C, while if the graphene substrate was heated up to 500–700°C, the diffusing free C atoms were more likely to form sp^2 bonds with the step-edge C-atoms of graphene, leading to in-plane graphene

growth. On the other hand, raising the temperature above 700°C caused the etching effect to be dominant over the carbon adsorption, so that no growth was observed.

Given the significance of the etching and curing effects in the graphene layer at high temperatures [47, 48], Kano et al. [49] investigated the structure and dynamics of Cu atoms embedded in single-layer graphene by aberration-corrected TEM operating at 80 kV while heating the sample through a MEMS-based chip. Cu atoms could replace C atoms of graphene under irradiation by a focused electron beam, more easily when residual oxygen and hydrocarbon contaminations were present. However, the Cu-C substitution was in competition with Cu evaporation: analyzing these processes during *in situ* annealing led to finding a threshold value with substitution being favored up to 300°C and Cu evaporation leading at higher temperatures. Then, choosing adequate electron beam currents and annealing temperatures allowed a control over the density of Cu-C substitutions. In particular, observations at 150 and 300°C showed that the Cu substitution led to local straining of graphene. These observations suggested that Cu atoms tended to combine with SW defects (Stone-Wales defects, i.e., pairs of five- and seven-membered rings at a 30° grain boundary [50]) forming grain boundaries between the reconstructed and original grains and, preferentially, replacing C atoms in defective graphene areas. Thus, the substitution modified the lattice structure by promoting C-C bond rotation, formation and mending of nanopores and rotation of grains mediated by defects (**Figure 4B**). In turn, this caused the disruption of grains in the graphene and its reconstruction as a less-strained lattice. So, unlike metals such as Cr, Ti, Pd, Ni, and Al, whose presence determines an etching of graphene, the presence of individual Cu atoms can catalyze a curing effect of graphene [51].
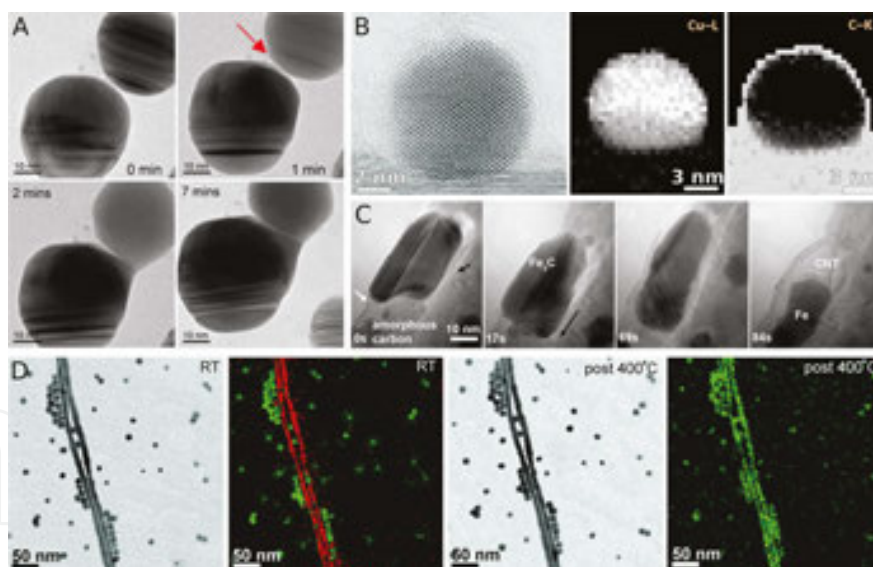

Figure 4. (A) Sequential ADF (annular dark-field) images showing graphene from the step edge of the BLG at 500°C. The dashed magenta line indicates the initial 2nd layer step edge, while the cyan dot line highlights the rotated 2+ layer. Green arrows show the single Si atoms at the step edge and a white arrow indicates the pinned Si atom. Adapted with permission from [45]; (B) representative TEM images taken before (left) and after (right) the reconstruction of graphene at 150°C. Insets show the FFT images. Adapted with permission from [49]; (C) representative TEM images showing the evolution of a graphene nanopore with varying temperatures. Adapted with permission from [55]; (D) nanopore sizes control, showing selected frames of electron beam hole sputtering at 800°C (left) and nanopores shrinkage at room temperature (right). Variations in the nanopores area trend are presented along with a linear fit in the graphs beside the frames. Adapted with permission from [55].

The effects of temperature on graphene are not limited to the cleaning and restoration of the lattice: in fact, those same temperature-dependent effects can be exploited to perform nano-fabrication. Nanopores embedded in thin membranes attracted special interest for their potential application in label-free, single-molecule detection of chemicals or biomolecules [52, 53]. Xu showed that a strongly focused 300 kV electron beam could be used to sculpt free-standing monolayer graphene with close-to-atomic precision in the STEM mode while heating the sample at 600°C [54]. The same electron beam with different scanning dwell times was used for sculpting and imaging: this allowed an immediate switching between sculpting and imaging and consequently fine-tuning the shape of the sculpted lattice. The effect of temperature was clarified by performing sculpting at 20, 400, 600, 700, and 800°C under identical STEM conditions while varying dwell times. The sculpting was successfully performed between 400 and 700°C, but it led to the contamination of the specimen at 20°C and it was not possible, even with large dwell time, at 800°C likely due to self-repair process being faster than C removal. More in detail, the experiment consisted in three steps: preparation, sculpturing, and inspection. The preparation of the sculpting area was performed in imaging mode at 600°C so that any isolated defects created by the electron beam were removed by self-repair of the lattice. Then, in sculpting mode, using a longer dwell time, several adjacent carbon atoms were knocked-out to prevent self-repair of the graphene lattice; extending the initial hole in a predefined direction it was possible to shape the graphene in a pattern with a precise position, size, and orientation. Finally, switching again to the imaging mode the sculpted pattern was inspected without introducing damages. Furthermore, the patterned graphene nanostructures were stable after being cooled to room temperature and stored in air. He also studied the stability of nanopores, developing a method to eliminate the dangling bonds at the pores edge in monolayer graphene and creating the so-called closed edge nanopores by using electron beam irradiation during *in situ* annealing and leading to pores that were stable for up to 2 days in air [55]. The process, taking advantage of the fast temperature ramps of MEMS-based holders, could be divided into four steps: the nanopores were first created by focusing of the electron beam at 800°C, with a subsequent cooling at room temperature to aggregate and fix the hydrocarbon adsorbates to their edges; a subsequent second heating to 800°C led to the crystallization of hydrocarbons to form closed edges around the pores, while a final cooling to room temperature stabilized the newly formed pores. As for the study of Xu, this process was strongly dependent on precise values of temperature (**Figure 4C**) and time (**Figure 4D**), but all these studies demonstrate how recent advances of *in situ* TEM annealing introduce the possibility to investigate in real time and at atomic scale the relationships between structure, properties, and functionality of graphene, which are essential in tailoring or designing devices based on this promising carbon-based material.

2.4. New directions and perspectives of *in situ* TEM annealing

The resurgence of *in situ* techniques due to the technological advancements experienced in recent years allowed an improved/deeper understanding of a vast range of processes at atomic scale, but other than pushing forward along already established routes also offered a chance for branching toward new directions.

A couple of recent studies dealing with the role of carbon with regard to *in situ* reactions from different aspects proved a good point in this matter. Carbon, as a support film of TEM grids or as an undesired presence inside the TEM column (e.g., hydrocarbon, which can be encountered as residues in the TEM column [45] or as a capping agent of NPs) is widely known to be a possible "active player" in annealing reactions. In particular, the role of carbon as a capping agent was the main focus of a study by Asoro, who successfully accounted for its role during sintering [56]. By performing *in situ* annealing experiments on carbon-covered Ag NPs of different sizes and origins and comparing the resulting diffusivity values with analogous experiments involving carbon-covered Ag NPs on a micrometric Ag wire, they observed that the formation of a neck bridging adjacent NPs is opposed by the presence of carbon coating, which acts as a steric barrier to its formation and, consequently, to sintering. In fact, the interparticle diffusion of Ag atoms must occur through the carbon: the formation of the Ag neck determines the out-diffusion of C atoms from the contact region, but also a decrease in diffusivity during ripening processes at the nanoscale (**Figure 5A**). The role of carbon capping to phase transitions during annealing experiments was also the main focus of a study conducted by Chen et al. [57]. By comparing the results of *in situ* annealing experiments performed on carbon- or Cu_2O-supported Cu NPs, different melting conditions were observed. The melting point of Cu NPs on Cu_2O substrates was 100 K lower than its counterpart for Cu NPs on a carbon substrate and the reason of this discrepancy in thermal stability was attributed to the presence of a coating layer of carbon adsorbed on the surface of the NPs and acting as a

Figure 5. (A) TEM images collected during *in situ* heating at 300°C, showing that the carbon residue on the surface of two sintering Ag NPs can prevent neck growth. Adapted with permission from [56]; (B) a typical Cu NP supported on graphite with a thin amorphous layer on its surface. Core-loss images of C-K and Cu-L edges confirm the presence of a 1 nm thick amorphous layer identified as C. Adapted with permission from [57]; (C) *in situ* TEM observations of the nucleation and growth of a CNT from an Fe_2O_3 catalyst NP, showing the evolution of the NP along with the dissolution of amorphous carbon and the growth of the CNT. Adapted with permission from [59]; (D) sequence of elastic-filtered TEM images and normalized EFTEM maps of $Cu_{2-x}Se$ NPs and CdSe NWs recorded at RT and postthermal treatment at 400°C. Green and red color coding indicates the presence of Cu and Cd in the EFTEM maps, respectively. Adapted with permission from [61].

thermal shield (**Figure 5B**). Core loss EELS mapping of C and Cu proved the presence of the C coating layer, while molecular dynamics simulations confirmed its shielding effect on Cu NPs, thus showing how "external factors" should be taken into account to explain discrepancies usually observed at the nanoscale.

Romankov and Park [58] approached the problem of C contribution to *in situ* annealing experiments from a very different starting point, i.e., structural studies and evolution of nanolaminated composite materials against temperature, and suggested an unconventional use of the carbon layer. By annealing a crystalline/amorphous nanocomposite (CoFeNi/Cu/ZrAlO)/C/W lamellar sample, they took advantage of the intermediate amorphous C layer to observe the out-diffusion of atomic species from all the layers and uses it as an *in situ* "reaction chamber" where those species could form new HSs or grow new phases. Moreover, the complex, liquid-like diffusion of CoFeNi at the C/CoFeNi interface was observed. During the annealing, the interfacial atoms from the highly disordered layers of CoFeNi were attracted by the carbon surfaces of the pores, which led to the lengthening of branches formed by a disordered shell and an ordered core and their diffusion through the carbon layer. Carbon is then a suitable candidate in the fabrication of nanocomposite structures or as a porous matrix for *in situ* observation of liquid-solid reactions.

Recently, *in situ* TEM annealing was also used to shed new light on some fundamental phenomena that have been generally accepted but never investigated in detail at the nanoscale, such as the nucleation, growth, and transformation processes of various well-known nanostructures.

A good example is given by carbon nanotubes (CNTs), which lacked a detailed nucleation study, despite their popularity for many possible applications. While their nucleation was generally ascribed to a generic vapor-liquid-solid (VLS) mechanism, the study conducted by Tang et al. [59] was specifically focused on shedding light on these aspects. The nucleation and growth of CNTs were studied by using an unconventional *in situ* annealing setup composed by poorly crystalized CNTs containing the catalytic NPs (Fe_2O_3 or Au) and acting as crucibles. The CNTs, also acting as C reservoirs for the growth of new nanotubes, were connected to electrodes and the system was annealed by heating the CNTs by Joule effect. During the annealing, the Fe_2O_3 NPs interacted with carbon from the CNT to form the Fe_3C catalyst, which triggered the nucleation of new CNTs and in turn transformed in metallic Fe once the CNT growth had stopped (**Figure 5C**). Moreover, *in situ* TEM showed the actual evolution of the Fe_3C and Au nanocatalysts during CNT nucleation and growth with the NPs going through multiple intermediate physical states that could not be reconducted to the simple, previously derived VLS model. Boston adopted a similar approach with a MEMS-based setup to investigate the nucleation and growth of quaternary Y_2BaCuO_5 nanowires (NWs) by a microcrucible mechanism [60]. Freezing the NW growth by rapidly cooling the system, the molten $BaCO_3$ NPs were observed diffusing on the surface of the porous precursor matrix to form an amorphous region at the base of the NW. This region, containing a mixture of the constituting elements of the NWs, was identified as the actual microcrucible, with the $BaCO_3$ NPs collecting the other cations by solubilization while diffusing on the matrix. Given the dynamic nature of the liquid/solid interface between microcrucible and NW, the shape and size of the microcru-

cible was expected to change with the NW growth and its evolution was studied by *in situ* annealing. Therefore, the direct TEM observation of the microcrucible creep with the NW growth during the *in situ* annealing showed how variations in the microcrucible modify the shape, size, and crystallinity of the NW, thus offering new insight into the growth of complex NWs.

The study of Casu et al. [61] provides a further example, focusing on modifications occurring during CE reactions in solid state at the nanoscale during *in situ* TEM annealing. In fact, while the out-diffusion and motion of chemical species have previously been accounted for as a generic possibility during *in situ* exchange reactions happening at the nanoscale, it was never actively investigated or used as a tool for *in situ* ionic exchange reactions. Taking advantage of the temperature-dependent copper depletion of Cu_2Se NPs, CE reactions were studied between two distinct populations of metallic Cu/Cu_2Se NPs and CdSe NRs/NWs with the TEM grid substrate acting as a medium for the Cu diffusion. Upon *in situ* annealing of Cu-containing and CdSe NPs, a CE reaction was observed in the latter, with Cu completely substituting Cd (**Figure 5D**). The structural and chemical data collected during the thermal-driven CE reactions proved that the kinetics of solid-state CE was slower than those of CE occurring in solution, therefore allowing the direct observation of the structural modifications occurring to CdSe upon CE. These observations showed a novel route for CE reactions at the solid state, while the slower kinetics offer a chance to study the intermediate steps that cannot be observed for CE reactions performed in solution.

3. *In situ* gas-solid reactions in environmental (S)TEM

Chemical reactions between gaseous phases and solid materials represent a challenging topic not only for the basic scientific research but also for important industrial applications. Since the dawn of the TEM technique, scientists tried to locally modify the environment around the specimen by introducing liquid or gaseous phases in order to study the materials under reactive or real environments [62–64]. These attempts clashed with the "classical" configuration of the TEM, which normally needs high vacuum conditions (1×10^{-7} Torr) [65] to protect the electron gun, to prevent contamination of the sample, and to avoid any blurring effect due to additional scattering of the electron beam with atoms that are not part of the specimen. The challenge was then to increase the gas pressure in a localized and controlled environment around the specimen so that temperature, gas composition, and pressure could be tuned without compromising the performance of the microscope itself. Scientists and manufactures developed two confinement methods for gaseous phases to achieve controlled environment TEM (E-TEM): (i) differentially pumped systems, featuring modified TEM column and vacuum system [66–72], and (ii) window-closed cells designed *ad hoc* to fit in TEM holders [73–77]. Neither of these methods requires special protocols for specimen preparation and both allow investigation by the usual TEM and STEM techniques [78].

Nowadays, coupling these two methods with the exceptional spatial and time resolution capabilities of state-of-the-art (S)TEMs and detectors, such as those used in EDS and EELS,

creates an extremely powerful tool for structural and chemical analyses of materials up to the atomic scale and over the reaction time [79]. However, the introduction of gases to create an environmental cell inside the TEM implies some additional limitations, i.e., the degradation of signal and spatial resolutions. The presence of an external gas species implies a direct rise in the number of molecules along the path L of the electron beam in the vicinity of the specimen and, in turn, is responsible for additional scattering events (*extrinsic scattering*) [80]. Although *extrinsic scattering* can present additional contributions coming from the interaction of electrons with the confining thin windows in the case of window-closed cells, the main contribution usually comes from interaction with gases, so the number (*m*) of *extrinsic scattering* varies proportionally to the gas pressure and the *m* value can be calculated considering the number of *extrinsic scattering* events within a cylindrical volume, defined by scattering cross section (σ) and length of electrons path (*L*) as expressed in Eq. (1):

$$m = \frac{LPM\sigma}{k_{\mathrm{B}}T} \tag{1}$$

where σ is the mass density of the gas, *P* is the gas pressure, *M* is the number of atoms per gas molecule, k_{B} is the Boltzmann's constant, and *T* is the temperature. The *extrinsic scattering* causes an overall reduction of the signal-to-noise ratio, followed by a progressive blurring effect and worsening of spatial resolution, since any imaging (textural and structural data) and spectroscopic (chemical data) information correlated to the specimen will be forwarded only by those electrons which did not undergo *extrinsic scattering* [80]. Hence, the forwarded signals can go through the TEM column toward the different types of detectors for recording and analysis processes.
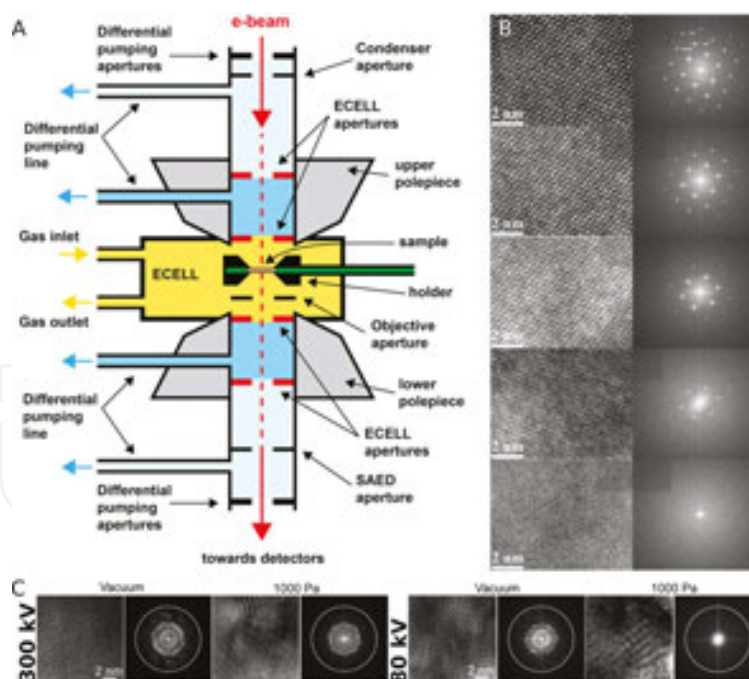
3.1. The differentially pumped system

The differentially pumped system approach relies on a modified TEM setup to perform environmental studies. In this case, the environment cell (E-Cell), generally intended as the experimental chamber where the specimen comes in contact with user-introduced gaseous species, is constituted by the portion of TEM column around the sample that is limited by a double series of additional apertures with small holes, which are positioned in correspondence with the objective lens pole pieces to confine the gaseous phases. Two additional sets of apertures along the column combined to a differential pumping system create zones of decreasing pressure between the high pressure zone of the E-Cell and the high vacuum of the other parts of the TEM column, thus protecting the electron gun from any gas coming from the E-Cell (**Figure 6A**).

This architecture allows the separate vacuum control of the E-Cell from the rest of the TEM column so that all the volume around the sample delimited by the objective lens can be filled with gases at low pressure and evacuated independently. The introduction of external gases implies that the E-Cell needs to be connected to an external gas manifold and flow controller system equipped with gas reservoir tanks, unreactive pipelines, and pressure gauges for any

tuning and monitoring procedures [71] but no modification is necessary with regard to the holder and any type of tilting and heating TEM holders can be used to perform *in situ* experiments.

The main advantage of the differential pumping is that it is an *open* system, meaning that the electron scattering comes only from the sample and the gas molecules, while no containment window is needed, although it is also worth noting that this architecture can reach only limited pressure values (around 20 Torr) without jeopardizing the TEM and electron gun [81]. However, this solution comes with a cost, i.e., the blocking of electrons scattered at high angle by the lower series of differential apertures below the sample [67]. This constraint imposes a strong limitation to the capabilities of different analytical techniques, e.g., STEM imaging by annular dark field (ADF) and high angle annular dark field (HAADF) detectors, electron diffraction of patterns collected at high angle [82, 83], and EELS, since the range of collection semiangle of the spectrometer cannot exceed the angular value of the lower E-Cell and differentially pumped apertures. Moreover, the introduction of a differentially pumped system results in a more complex and more expensive system.

In addition, the imaging resolution is not only affected by the presence of gases, but it is also influenced by additional electro-optical and microscope-related parameters with opposite effects, i.e., the electron dose and the primary electron energy. In fact, under the same conditions of E-Cell gas pressure and primary high tension, reducing the electron-dose increases
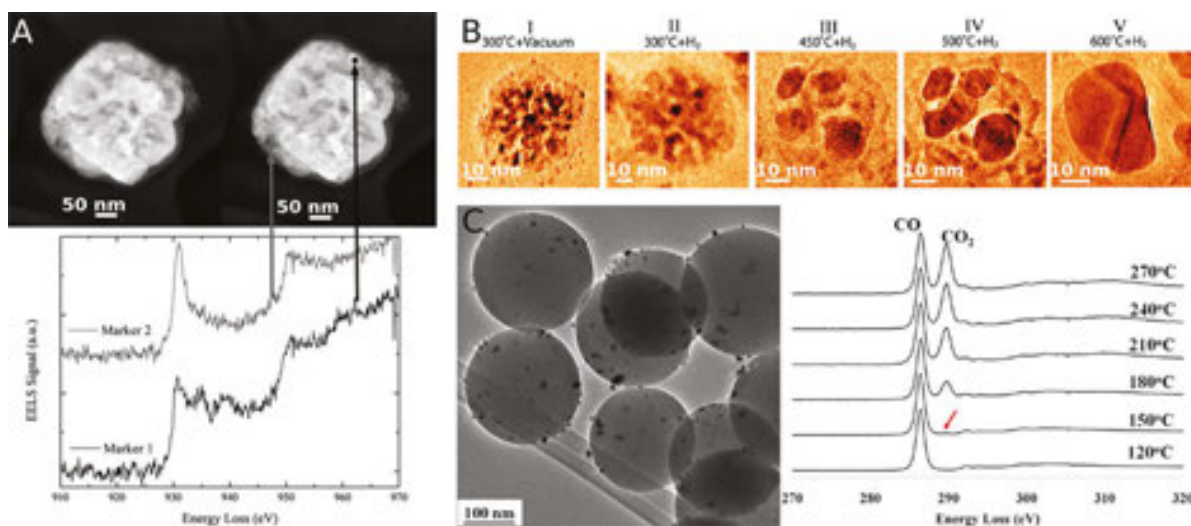

Figure 6. (A) Schema of a differentially pumped TEM system after [71]; (B) sequence of HRTEM images and the corresponding diffractograms of an Si 011 crystal lattice measured under 4 mbar of N_2 gas pressure and different electron doses. Adapted with permission from [84]; (C) HRTEM and the corresponding power spectrum of an Au film on carbon film, showing the pressure dependence of the transmitted information limit under different conditions of acceleration tension and N_2 gas pressure. The white circle corresponds to 10 nm^{-1}. Adapted with permission from [85].

the spatial resolution (**Figure 6B**) [84], while reducing the high tension worsens the spatial resolution (**Figure 6C**) [85]. These effects can be explained thinking that a low electron dose will lower the electron density of the beam and the overall number of *extrinsic scattering* events, while, on the other hand, a lower tension will induce a stronger scattering effect between the electron beam and the atoms of the sample and the gas molecules, the latter resulting in a worsening of the signal-to-noise ratio [86]. Therefore, a proper evaluation of the best setting of the microscope according to the type of material, gas phase, pressure, and chemical reaction to be studied is mandatory before starting any experiment of environmental (S)TEM.

In general, the combination of *open* architecture and limited *extrinsic scattering* contributions due to the use of low working pressures make the open E-Cell suitable for chemical investigations of materials through EELS analysis. For these reasons, many recent basic and applicative studies of catalytic materials took advantage of this combination to study the structural and textural modifications of NPs exposed to reactive gas, following their change of valence state via EELS near-edge fine structure analysis.

In particular, studying the modifications occurring to catalysts in different temperature and pressure regimes is a focal point for assessing the best working conditions and comprehending variations in catalytic performance. This is the case of cuprous oxide (Cu_2O) NPs, which represents an active photocatalyst for hydrogen production by water splitting through direct irradiation with visible light ($\lambda > 400$ nm) [87]. Studying the variations in the oxidation state of copper on Cu_2O nanocubes under water vapor (5 mbar) and light exposure ($\lambda = 405$ nm) (**Figure 7A**) by EELS near-edge structure analysis of the Cu $L_{2,3}$ edge highlighted a variation in the near-edge features throughout the photocatalytic reaction. In fact, the two strong L_2 and L_3 ionization edges—"white lines"—showed by oxidized copper (Cu^+, Cu^{2+}) at 951 and 931 eV, respectively, were substituted by one step-like abrupt onset of L_3 edge followed by weak features, which is typical of metallic copper (Cu^0) and revealed that the photocatalytic reaction also led to a self-degradation process of the NPs to metallic Cu. Another example is offered by the study on the evolution of Ni NPs during oxidation [88]. In fact, Ni is a viable catalyst for a wide range of applications, including energy production in solid fuel cells, but its oxidation leads to a lessening of its catalytic performance. Therefore, analyzing in detail by *in situ* E-TEM the structural and chemical transformations induced by oxidation to crystallites represents a first step in understanding and, possibly, control this process. In particular, the comparison of structural and chemical data showed that the oxidation process progressed as the pervasive formation of a thin NiO layer covering the Ni NPs, and subsequently growing at the expense of the Ni component by increasing the temperature, until the final evolution into porous, polycrystalline NiO structures, which are responsible for the worsened catalytic performance. Xin used a similar approach to monitor the transformation of nanoporous CoO_x/silica nanocomposites under H_2 flux at different temperatures [89]. In fact, while the chemical analysis of the Co $L_{2,3}$ edge of EELS signal exhibits a clear fingerprint of reduction of Co valence from Co^{2+} to Co^0 during the exposure to H_2 at high temperatures, the *in situ* TEM showed a coarsening of the composites, reflected by an increase in size of the Co component at the expense of the composites porosity. This evidence translated in the quantification of a structural trend

from a porous nanosized network to solid NPs, which can be used to tailor the catalyst features in its actual working conditions (**Figure 7B**).

Figure 7. (A) HAADF STEM images of a Cu_2O nanocube before (left) and 30 min after (right) the photocatalytic reaction. The corresponding EEL spectra of the peripheral region (below) show the coexistence of metallic Cu portions (marker 1) in the Cu_2O nanocube (Marker 2). Adapted with permission from [87]; (B) *in situ* observation of structural changes of Co/CoO_x NPs under different reduction conditions and temperatures. Adapted with permission from [89]; (C) representative TEM image of Ru/SiO_2 NPs (left) and background subtracted EEL spectra acquired at different temperatures during the oxidation reaction of CO (right). Adapted with permission from [91].

On the other hand, E-TEM is also a powerful tool for direct observation in more applicative-inclined studies, devoted to test and observe the performance and limits of materials with more immediate practical repercussions. Such is the case of the study on yttria-stabilized zirconia (YSZ) NPs as a treatment device for soot exhaust products by their oxygen channeling capability [90]. *In situ* E-TEM experiments, conducted under high temperature conditions with a 3 mbar pressure of O_2 on a tight mix of YSZ and soot, offered direct evidence of the role of YSZ. In fact, the direct observation showed how the oxidation front of soot was indeed at the surface of the NPs, where the O^{2-} is made available, while soot particles not in contact with YSZ remained unaffected despite being surrounded by gaseous oxygen, thus confirming how the oxidation of carbon soot to CO_2 was due to the capability of YSZ of conducting O^{2-} ions toward the NPs surface and making them available for oxidation. Similarly, Chenna et Crozier [91] were able to detect and quantify the catalytic process in the E-TEM by EELS, showing the feasibility of an *Operando TEM* approach for simultaneous structural and reactivity studies. To achieve this goal, they investigated the oxidation effects of Ru/SiO_2 nanocomposites on CO gas. Taking advantage of the high catalytic performance of Ru/SiO_2 and of the variation of C π^* peak, going from 286.4 eV for CO to 289.7 eV for CO_2, they heated the sample and collected the EELS spectra during the oxidation of CO to CO_2. By monitoring the appearance and growth of the C π^* peak of CO_2 and the variation of its intensity with respect to the C π^* peak of CO, it was possible to confirm that the oxidation reaction was taking place to observe temperature-dependent variations in the oxidation (**Figure 7C**), thus showing the feasibility and power of the *Operando* approach in E-TEM.
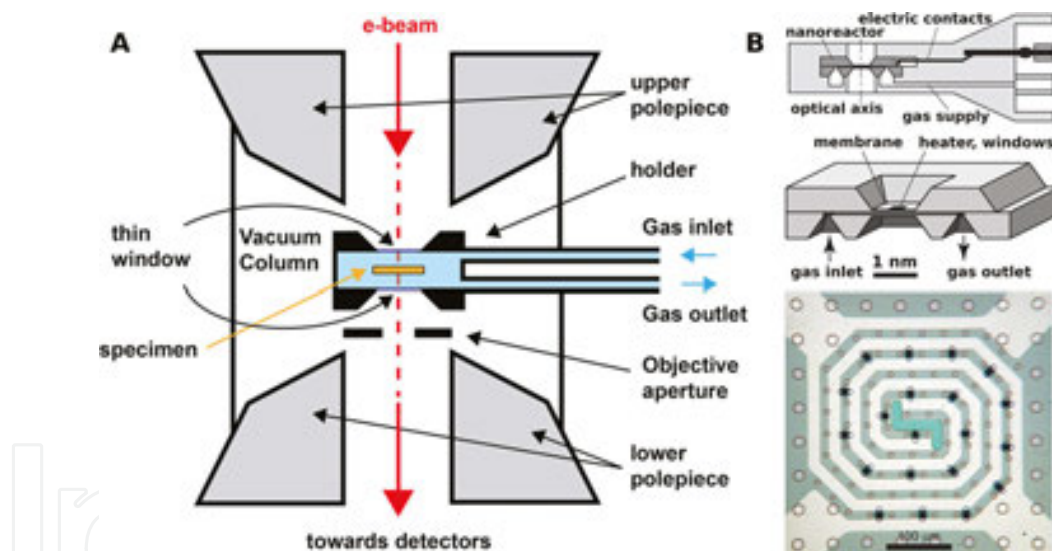
3.2. The window-closed E-cell

The window-closed cell is the main alternative to the differentially pumped system for environmental TEM analysis. In this case, the E-cell is incorporated into the tip of a dedicated TEM holder and uses two parallel electron-transparent windows to confine the sample and the gases inside a tiny-volume nanoreactor (**Figure 8A**), while no modification to the TEM column is required. By reducing the volume to a small, closed layer around the specimen, the gaseous phases can reach pressures above one atmosphere [92–94], while the nanoreactor can be safely inserted in the TEM column. The main advantage, other than the higher working pressures, is that this setup can be installed in different TEMs without any modification to the column and vacuum system with a direct saving of costs of purchasing and maintenance.

The confinement diaphragms of the window-closed cell must have some fundamental prerequisites. Namely, they must (i) be electron-transparent, (ii) be strong enough to confine the pressurized gas, and (iii) provide a low diffraction contribution in order to reduce any effects of diffraction contrast and limit the superposition of additional periodic patterns to the "proper" signals coming from the sample [95]. These are the reasons why the diaphragms are made of thin and amorphous materials with low average atomic number (e.g., carbon, silicon nitride), thus also minimizing their *extrinsic scattering* contribution [95]. However, the additional contributions of diaphragms to the *extrinsic scattering* can increase the energy spread of primary electrons, resulting in a worsening of spatial resolution of both the microscope [75] and EELS capabilities because of a stronger damping effect on contrast transfer function and a worse energy spread of the beam entering the specimen, respectively. In a similar fashion, the escape of any X-ray signals generated during the scattering events between primary electrons and sample atoms will be partially or totally absorbed by the diaphragms [92]. The "closed" nature of this setup does not require any additional apertures in the lower part of objective lens and column, thus making available to the detectors the forwarded signals coming from electrons scattered at high angle and removing some of the limitations encountered in the differentially pumped systems. However, the gas path length between the windows is still a crucial parameter: the spatial resolution displays an overall worsening under high-pressure conditions (1 atm) in nanoreactors with thin windows but longer gas paths (more than 1 mm), due to the dramatic increase in the number of *extrinsic scattering* events [96], akin to the differentially pumped systems.

Also, in this configuration the gas pressure and the temperature inside the cell can be monitored and varied continuously, up to the instrumental limit. The holder is generally connected to an external gas line equipped with gas reservoir tanks, unreactive pipelines, and manometer pressure gauges capable to control the pressure from few mbars to few bars, while a dedicated vacuum pump is used for purging operations [93].

In this regard, the introduction of micromechanical system (MEMS) technology led to important improvements in the mechanical characteristics, design, and performance of window materials and in the engineering of holders with respect to previously available setups (**Figure 8B**) [92, 94, 97]. The last generations of closed cell nanoreactors, obtained via MEMS technology, integrate electron-transparent diaphragms made of 10 nm thick amorphous silicon nitride, flow gas pipes of a few tens of micrometer wide, micropressure controlling gauges,

and microheaters [98, 99]. Usually, the heater system is a metallic spiral strip (e.g., underdoped Pt or Pt-based alloys) embedded on the lower thin window and the gas path between the windows is in the order of some tens of micrometers, which allows a reduction in the volume of the cell. Moreover, the spiral shape of the heater helps to minimize any spurious magnetic fields interfering with those of the electromagnetic lenses [98] and any thermal gradient upon the sample. The combination of these parameters makes MEMS-based nanoreactors suitable for HRTEM and HRSTEM imaging in Cs-corrected microscopes even at atomic scale, as demonstrated, e.g., by the study of Allard et al. [93] on catalytic nanomaterials, which exhibited atomic columns resolution under vacuum in Au NPs grown on Fe_2O_3 and in Rh nanocrystals on $CaTiO_3$ under pressures up to 1 atm. Ultimately, the improvement in performance over a wide range of working pressures and temperatures and the adaptability to different (S)TEMs without any modification of columns and vacuum systems provide the window-closed cells a high experimental flexibility, which makes them valuable in a variety of scientific studies devoted to the *in situ* observation of chemical reactions. Obviously, given the novelty of the most recent developments of the E-TEM technique, different technical approaches are being explored. While third-party solutions are already available in the market, many groups are also developing their own custom-built setups to perform environmental TEM experiments.
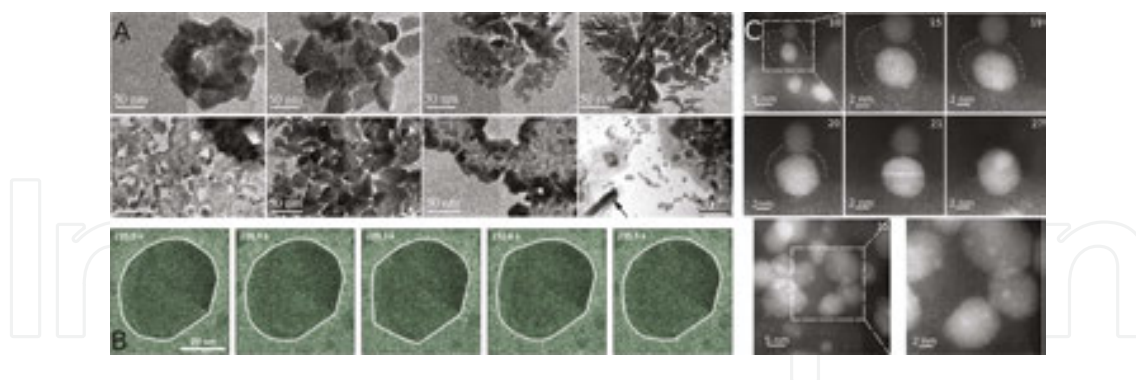

Figure 8. (A) Schema of TEM holder with window-closed cell; (B) MEMS-based nanoreactor. Top: Schematic lateral cross section with the electrical contact for the heater; middle: schematic 3D view of the MEMS nanoreactor; bottom: active area, featuring the microheater spiral (in white) with ovaloid electron-transparent windows and circular spacers. Adapted with permission from [92].

In this context, Sun et al. adapted a wet cell they previously developed into a closed-cell setup for *in situ* E-TEM experiments devoted to observe the oxidation of Ag NPs in air [100]. Due to its ionizing effects on molecular oxygen, the electron beam was used to obtain atomic and ionic oxygen inside the E-Cell, which acted as ionizing agents for Ag. Therefore, variations in the electron beam current intensity were reflected in the oxidation reactions products: at first increases in current density were revealed by the progressive decrease in Ag NPs size

accompanied by the nucleation of new Ag and silver oxide grains; further increases in current density resulted in the progressive predominance of oxide over metallic silver with the heating effects of the electron beam having an increasingly prominent role. The melting of crystalline silver oxide due to beam heating led to the formation of a noncrystalline, highly dynamic vapor phase, which swept through the E-Cell either aligning to nucleate clusters of Ag NPs or dissolving NPs (**Figure 9A**).

More recently, Vendelbo et al. [97] used a MEMS-based nanoreactor to study *in situ* the oscillatory variations in the structure of catalytic Pt NPs during CO oxidation. In fact, while the oscillatory behavior of catalytic reactions under stable conditions was already known, the role of nanosized catalysts was still unclear. Experimental data were acquired while 1.0 bar of $CO/O_2/He$ was flowing through the E-Cell containing Pt NPs at a steady temperature of 659 K. The catalytic performance of the NPs was verified by measuring variations in mass spectrometry of the CO and CO_2 phases exiting the nanoreactor, while time-resolved HRTEM imaging recorded variations in the structure of the Pt NPs. Finally, calorimetric information about the chemical reaction was extracted by recording fluctuations in the electrical power consumption of the MEMS nanoreactor due to the heat released by the CO oxidation. By correlating the reaction data with the variations in morphology observed on the catalytic NPs, it was observed that a periodic and reversible faceting of Pt between a spherical and a facetted shape is indeed the cause of the periodic oscillations in these catalytic reactions (**Figure 9B**). In a similar fashion, the *in situ* study performed by Zhang et al. [101] on the evolution of Si-supported $Pd@CeO_2$ nanocatalysts revealed the presence of dynamical processes that altered drastically the structure of the nanocomposites and that could only be observed by closed cell *in situ* E-TEM. In fact, while the performance of $Pd@CeO_2$ was usually attributed to the formation of a core-shell structure, *in situ* calcination at 500°C in a 150 Torr O_2 atmosphere

Figure 9. (A) Metallic evolution of Ag NPs in an air-filled cell after exposure. Top, from left to right: after 0 s with 0.18 A cm^2 current density; after 20 s with 0.18 A cm^2 current density (a new grain is indicated by a white arrow); after 0 s with 0.44 A cm^2 current density; after 20 s with 0.44 A cm^2 current density. Bottom, from left to right: after 0 s with 0.66 A cm^2 current density; after 20 s with 0.66 A cm^2 current density; after 20 s with 0.72 A cm^2 current density; after 20 s with 0.8 A cm^2 current density (the black arrow marks the vertical alignment of the AgO vapor phase). Adapted with permission from [100]; (B) time-resolved TEM images of a Pt nanoparticle at the gas exit of the reaction zone. The elapsed time is indicated in the top left corner. Adapted with permission from [97]; (C) (top) disappearance of an atom cloud and growth of a nearby particle, with subsequent coalescence at 650°C in 150 Torr O_2. The atomic cloud is delimited by a dashed line; (bottom) appearance of subnanometric features. The elapsed time indicated in minutes is at the top right corner of each image. Adapted with permission from [101].

revealed the dissociation of the Pd and CeO_2 particles to atomic clouds. Subsequent calcinations lead to re-organization of the atomic species into bigger sized ceria and Pd NPs or to the nucleation of a new structure featuring very small, highly dispersed silica, Pd, and ceria (**Figure 9C**). Assuming a conventional catalytic behavior of the bigger particles, the exceptional catalytical performance of Pd@CeO_2 above 800°C was attributed to this new structure.

4. *In situ* (S)TEM imaging of liquid specimens

As mentioned in the Section 1, since the invention of the electron microscope, one of the main scientific challenges has always been the imaging of liquid or wet samples. Even if this is usually possible by using light/fluorescence/confocal microscopy, and even taking into account the most recent and dramatic resolution improvements achieved due to the super-resolution approaches [102], its resolution (currently less than 100 nm) is still far from that of any electron microscope and represents a strong limit for nanoscale analyses of liquid samples. That being said, this section deals with the methods and devices that allow to achieve much higher resolution of liquid/wet samples performing *in situ* TEM instead of light-microscopy-based imaging. Analogously to what described in the previous section, also here the term "E-Cell" will be used to simply define the volume in which the interaction between the liquid environment and the specimen of interest occurs, irrespective of the device used to allow this interaction to happen.

A brief historical overview looks helpful in understanding what were, since the first decades of electron microscopy, the main limitations related to the possibility to perform *in situ* TEM of specimens kept in a liquid environment. First, the liquid has to be isolated from the rest of the column, which being under vacuum conditions would give rise to an almost immediate liquid evaporation, unless it would have a very low vapor pressure, and to the concomitant loss of the high vacuum conditions. The first trials to realize an *in situ* specimen holder capable to locally isolate the liquid in an E-Cell was proposed in the works of Abrams and McBain [103, 104]. It can be basically described as a platinum cell containing the liquid sample and constituted by two parts that were glued together, each provided with a very small hole where a window was attached, the latter thin enough to allow the electron beam to pass through them and the internal part that contained the liquid. This kind of E-Cell was just put in a normal TEM holder instead of the grid. The material used to fabricate the 50 nm thin electron-transparent windows was called collodion, and it was basically constituted by nitrocellulose. In none of the two papers of Abrams and McBain is reported any EM image of a liquid sample (gold particles in water) imaged by using this *in situ* specimen holder, and the authors affirmed that this was due to the particles' too rapid-free Brownian movement in a liquid as fluid as water. It was needed waiting almost 30 years to read a further paper [105] in which Ernest Fullam showed a novel way to fabricate a wet E-Cell for TEM. The design of this latter cell basically followed that of Abrams and McBain, but Fullam indicated that one of the most important failure of the colleagues' previous cell was due to the material chosen to fabricate the thin windows: the nitrocellulose films were invariably broken by the pressure difference between inside and outside the E-Cell, once it was inserted in the TEM column. In fact, the

most important novelty shown by Fullam was the manner followed to fabricate the thin and electron-transparent windows, which were now constituted by a triple-layer film: Formvar and nitrocellulose separately cast from fresh solutions and deposited on 400 mesh copper TEM grids. Fullam estimated this configuration having a total thickness ranging from 30 to 40 nm and showed that it did not suddenly ruptured, allowing to image chromium hydroxide spheres in water suspension even if, despite the low magnification (5k) used, still in such a case the loss in spatial resolution due to the water electron scattering as well as once again to the Brownian movement of the particles suspended in water is clearly reported. To limit both these effects, only a possible solution was indicated: making the liquid thickness contained by the E-Cell as low as possible.

A further and strong novelty was then proposed in the work of Parsons [66], who described a new kind of experimental design to perform *in situ* TEM of liquid samples. It is the birth of the so-called environmental TEM (E-TEM) that consisted, and still consists, in a completely different type of E-Cell inside the column, the details of which have been already described in the previous section. Basically, and to remind its working principle, this kind of E-Cell is no longer physically limited by two thin electron-transparent windows and then just inserted into the TEM column as a part of a special specimen holder, but it is itself a part of the TEM column, where the ability to kept it under low gaseous pressure conditions is given by a system constituted by two differentially pumped and apertures' limited volumes put just above and below the E-TEM cell. Parson indicated that in the E-TEM cell he proposed a water vapor pressure of around 0.03 bar was enough to establish and keep a wet compartment. However, by using such a configuration he also mentioned that a maximum resolution of about 4.0 nm in the presence of water vapor pressure could be attainable, with the microscope operating at an acceleration voltage of 200 kV, and showed an E-TEM image of unstained and unfixed coliform bacteria and intracytoplasmic organelles, even if not highly resolved.

A variation of E-TEM is that shown by Gai in [106], where both environmental and high-resolution TEM (EHRTEM) were shown with a double possible configuration: first, a specific microreactor inserted inside the E-Cell of the EHRTEM column enables studies of thermally driven gas-solid reactions, while keeping an atomic resolution. Similarly, a way to develop *in situ* TEM studies of wet samples that could be even heated was indicated. It consisted in inserting a dedicated specimen holder in the E-Cell, capable to inject liquids onto the sample, located in the furnace of the holder.

However, what was mainly developed in the following years and so far to perform *in situ* TEM imaging is mainly based on sample holders with the isolating double thin window systems. This is not only due to the not secondary point that purchasing an E-TEM is obviously much more expensive than acquiring a dedicated sample holder to be inserted into a conventional S(TEM). However, it was actually shown that *in situ* E-TEM imaging of liquid/wet specimen unavoidably brings to work with a liquid film thickness not less than 1 μm and whose fine control is very hardy achievable as a consequence of a high and systematic loss in the final point resolution.

More recently, double window-based E-Cells for liquids were then and again used for *in situ* specimen holders' fabrication, being adaptable to any standard. The sample of interest can be

sealed inside the double thin-window E-Cell together with gases or liquids, the latter possibly also let to flow. Although the E-Cell thin windows' presence unavoidably makes a little worse the final resolution, by such a way the sample can be surrounded by a thin gaseous or liquid environmental layer, with a thickness that can be *a priori* chosen within a large range, providing more or less resolution depending on both the chosen TEM imaging geometries and the total thickness of both sealing windows and interposed sample [107, 108].

The major improvement achieved for the development of specimen holders capable to allow *in situ* (S)TEM imaging of liquid samples was the fabrication of devices with robust but thin windows for the relevant E-Cells. These were realized producing thick microchips of amorphous silicon nitride (SiN) with a central zone having a thin or a very thin thickness (20–100 nm). In addition, further specific advances in the microchip fabrication allowed the integration of electrodes and microfluidic circuits to mimic physiological and/or dynamic conditions in the E-Cell for more specific *in situ* (S)TEM imaging such as, just for instance, the one of proteins or NPs interactions with whole cells [107, 109, 110], electrochemical reactions [111, 112], nanocrystals' growth in liquid solution [113, 114].

In the following, we first deal with the equations needed to determine the final point resolution when an *in situ* sample holder containing a water layer of given thickness is used in both TEM and STEM geometries since each of them brings to the optimal way to prepare the specimen that should be looked at. Second, it will continue and end with some examples of *in situ* (S)TEM imaging for both materials and biological science studies.

4.1. The point resolution when using an *in situ* sample holder for liquids
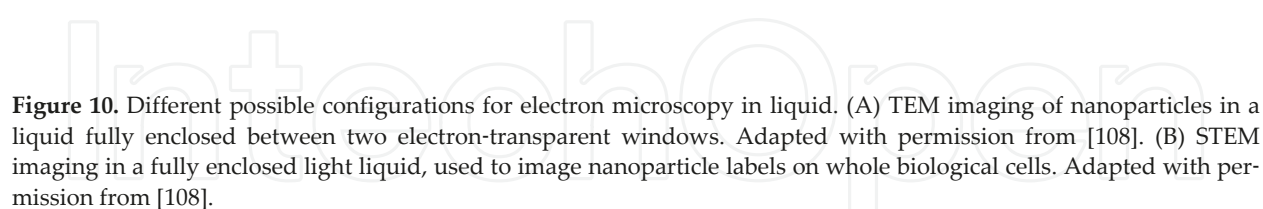
4.1.1. TEM

To determine how to calculate the final point resolution when using an *in situ* sample holder for liquids, a first approximation could be adopted. It consists in considering the material constituting the E-Cell windows with a scattering factor negligible for typical beam energies (200–300 keV), with respect to that of the liquid layer contained in the E-Cell, which is valid for most of the cases. Under such a condition, the main resolution's limiting factor is the chromatic aberration due to the inelastic scattering of electrons by the liquid. Taking then into account the most diffused and simple case of water as liquid medium, the electron energy broadening due to the beam-water inelastic scattering and the fact that chromatic aberration is the one effectively governing the final resolution, then d_{TEM} could be expressed by the following equation:

$$d_{\text{TEM}} = 6 \times 10^{12} \left(\frac{\alpha C_{\text{C}} T}{E^2} \right) \tag{2}$$

where C_C is the spherical aberration of the objective lens, usually ranging between 0.5 and 2 mm depending on the microscope used, α is the objective semi angle, E is the beam energy, and T is the whole thickness of the cell filled by water. The water features (density, mean atomic

number, and atomic weight) have been taken into account in the numerical coefficient appearing in the equation. Just for instance, with E = 200 keV, α = 10 mrad, C_C = 2mm, and T =1 μm, a final resolution d_{TEM} of 4 nm is calculated [108].

Thus, taking into account what indicated by Eq. (2) to look at any liquid sample (i.e., at a solid sample surrounded by a liquid environment) by TEM using the parallel electron beam geometry, the highest attainable resolution is obtained for solid objects surrounded by liquid in a configuration where electrons have to pass the lowest possible liquid volume after having crossed the solid objects, in order to minimize the energy broadening that they suffer in scattering with the liquid's molecules. For this reason, the solid part of the sample should be put onto the internal side of that E-Cell windows from which the electrons definitely exit from the E-Cell or, analogously, if the solid objects are homogeneously distributed all over the liquid the best choice to image them by TEM is that to focalize the ones closest to the lower E-Cell's window. In other words, to obtain the best resolution, the objective lens focal plane should be placed as near as possible to the internal side of the lower E-Cell's window. **Figure 10A** shows this experimental configuration.

Figure 10. Different possible configurations for electron microscopy in liquid. (A) TEM imaging of nanoparticles in a liquid fully enclosed between two electron-transparent windows. Adapted with permission from [108]. (B) STEM imaging in a fully enclosed light liquid, used to image nanoparticle labels on whole biological cells. Adapted with permission from [108].

4.1.2. STEM

Differently from the TEM geometry, in which a parallel electron beam is used to illuminate whole areas of the sample, in the STEM the imaging is performed by a convergent beam that scans the sample point by point and where the contrast is then obtained by collecting the electron signal produced by each irradiated point with an appropriate detector. Even considering that the transmitted beam is the simplest way to form an image (the so-called Bright field mode), to image the contrast due to small but atomically heavy objects (like NPs) dispersed in

a lighter liquid medium, the signal emitted with an high angle of divergence is usually the one collected to form the STEM image, being this STEM detection's geometry called HAADF. In such a case, the contrast is due to the fact that the detected signal's intensity is roughly proportional to Z^2, with Z being the atomic number of the material irradiated by the electron beam. Under these experimental conditions, the STEM resolution (d_{STEM}) achievable for a NPs' sample surrounded by a liquid environment is usually defined as the diameter of the smallest NP visible above the background noise as given by the following equation:

$$d_{STEM} = 5l_{nanop}\sqrt{\frac{T}{N_0 l_{liquid}}} \tag{3}$$

where l_{nanop} and l_{liquid} are the mean free path length for elastic scattering of NP and surrounding liquid, respectively, N_0 is the number of incident electrons, and T is the whole thickness of the liquid cell [107, 108].

Thus, the highest resolution for the STEM imaging of an object within a liquid is achieved when the object is at the entrance side of the sample. Moreover, keeping the specimen holder filled with the same water volume, the NP STEM imaging will be performed with a resolution in principle quite higher than the one obtainable by using a TEM imaging.

According to Eq. (3), a gold NP (marker) with a 1.4 nm in diameter can be resolved on a water layer of $T = 5$ μm. For NPs positioned deeper in the liquid, imaging takes place with a blurred probe, but a resolution better than 10 nm is still achieved in the top 1 μm layer of the liquid. As previously illustrated for the TEM, **Figure 10B** shows the experimental configuration corresponding to the STEM geometry with an *in situ* sealed E-Cell for liquid specimens.
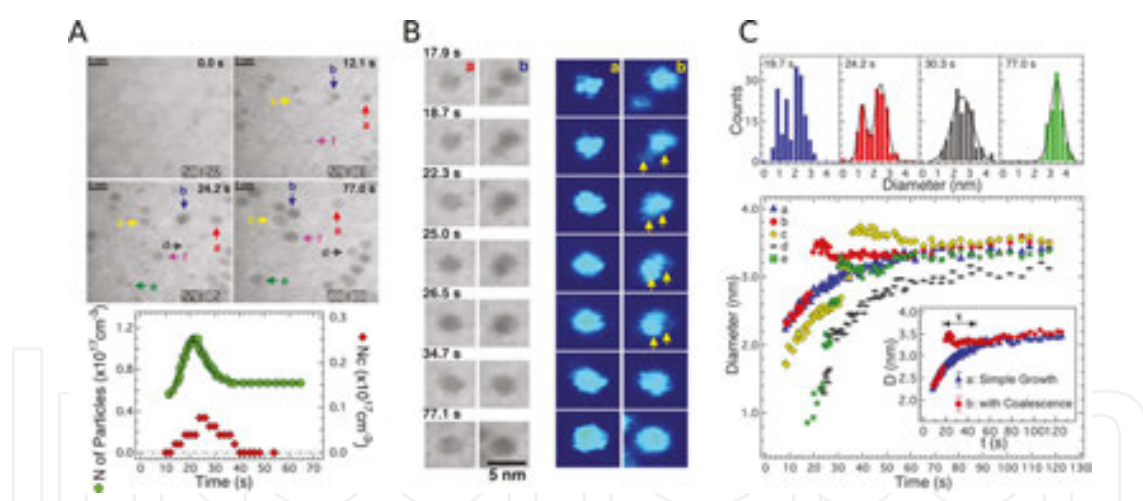
4.2. *In situ* liquid TEM for materials science studies

Just as short overview of the different fields of application of *in situ* (S)TEM of liquid sample and devices, in the following some quite known examples are reported. One of the important papers that started to show the terrific possibilities offered by this technique was that of Williamson et al. [111], while a quite similar study was also published by Radisic et al. [112]. Both works deal with electrochemical processes monitored over time by providing a sealed electrochemical E-Cell well fitted for both vacuum environment and restricted volume available in the TEM column. The liquid E-Cell is filled with a water-based solution (usually electrolytes) and also contains electrodes as shown in **Figure 11A**. Both papers showed time-resolved imaging of electrochemically driven process of nucleation and following growth of individual Cu clusters onto an electron-transparent Au electrode patterned over one of the windows of an E-TEM liquid cell, with simultaneous measurement of voltage and current involved. It should be noticed that in both papers the TEM operating mode and the corresponding beam geometry was chosen, and in fact the Cu nanoclusters' formation is observed when they reach a size of several tens of nanometers (**Figure 11B** and **C**).

Figure 11. (A) Sketch of the liquid cells' components. Adapted with permission from [111]. (B) The center-of-mass positions of Cu clusters during four deposition experiments (different colors) on the same area of the electrode. Inset is the micrograph that corresponds to the black circles. Adapted with permission from [111]. (C) Small regions extracted from a video recorded during deposition at 5 mA cm^{-2}. Images taken at the times shown after current flow began. Adapted with permission from [111].

In 2009, Zheng et al. again used TEM geometry and a double SiN window *in situ* E-Cell for liquid specimens to image Pt nanocrystals' growth and coalescence, obtaining a final resolution well lower than 1 nm, mainly due to the low spherical aberration of the high-resolution objective lens but also to the 200–300 kV accelerating voltage used [113]. For the particle synthesis, a stock solution was prepared by dissolving Pt(acetylacetonate)$_2$ in a mixture of *o*-dichlorobenzene and oleylamine. About 100 nanoliters of such a growth solution were put into

Figure 12. Growth and coalescence of Pt nanocrystals. (A) Top images: video frames acquired at different time points of exposure to the electron beam are reported, with specific particles labeled by arrows. Bottom image: the number of particles (left axis) and the number of coalescence events (Nc, right axis) vs. time, as measured with a time rate of 2.0 s. Adapted with permission from [113]. (B) Video images showing nanoparticle's growth occurred by monomer addition (left column, a) or growth by means of coalescence (left column, b). Particles are selected from the same field of view. Right columns (a) and (b): color images of the left ones, enlarged 1.5 times. The yellow arrows are indicating recrystallization observed in the coalesced particle. Adapted with permission from [113]. (C) Top images: histogram of particle size distribution at different time points, with black curves corresponding to Gaussian fittings. Bottom images: particle size vs. growth time of particles highlighted in panel (A). Inset shows two types of growth trajectories: simple growth and growth with coalescence. A relaxation time (τ) was observed after a coalescence event. Adapted with permission from [113].
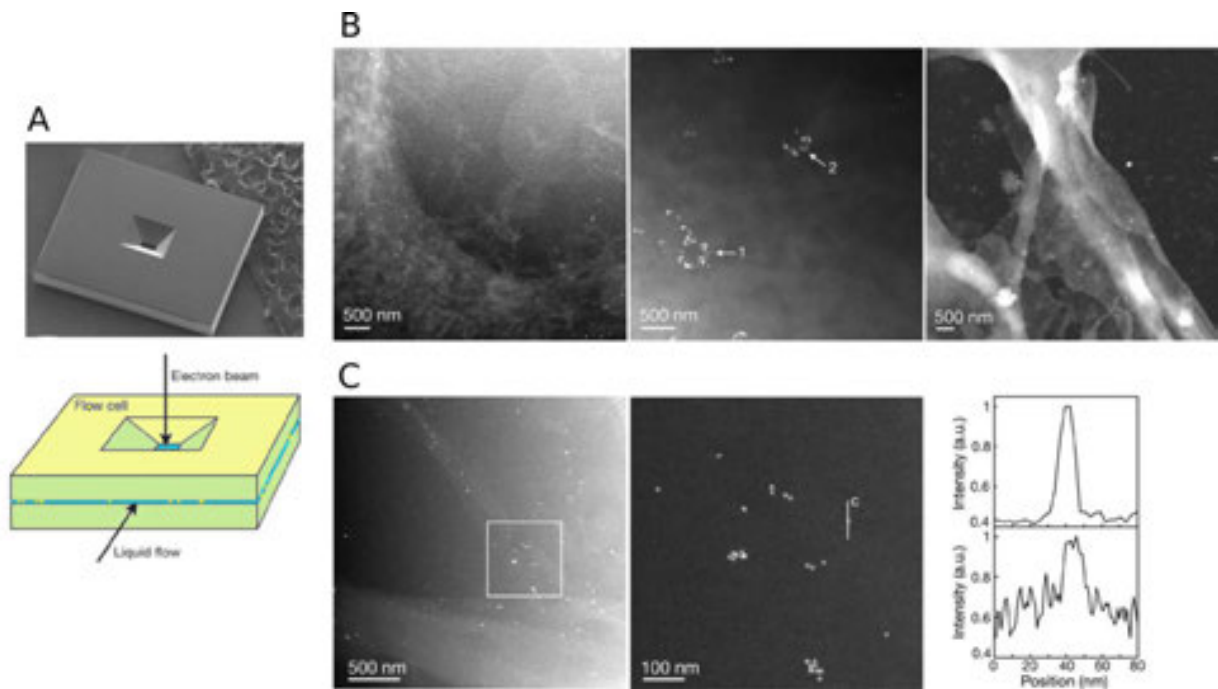
the E-Cell, where the SiN windows and the liquid layer had a thickness of 25 and 200 nm, respectively. It is crucial to highlight here that the driving force used to promote the nucleation, growth, and coalescence of the Pt NPs was the sole electron beam irradiation. The main results published in the paper of Zheng et al. are summarized in **Figure 12A–C**. They consisted in showing not only the nucleation and growth of the Pt nanoclusters over time in the sealed E-Cell, but also in showing the fundamental role played by the coalescence of the larger NPs with the smaller ones during the growth process.

Similarly to what cited above, Evans et al. synthesized PbS NPs using as electrolyte a solution containing lead acetate, poly(vinyl alcohol), isopropyl alcohol, and thioacetamide [114]. The selective decomposition of thioacetamide was again promoted using the illumination with high-energy electron beam as driving force, and it gave rise to the production of free sulfur ions in solution. Surrounding lead ions then reacted with the free sulfur ions to allow the PbS NPs to nucleate and grow, while the poly(vinyl alcohol) acted as a stabilizing agent. However, two quite important improvements were shown in the work of Evans et al. and consisted in (a) using a continuous flow of reactants, drawn in and out from the E-Cell by appropriate microfluidic lines and (b) monitoring the processes occurring inside the E-Cell by using a spherical aberration corrected STEM, with higher resolution than the one attainable using a conventional TEM, for the reasons explained above.

4.3. *In situ* liquid TEM for biological sciences studies

For biological purposes, both E-TEM and sealed E-Cells for liquid specimen holders have been used, with a large predominance of the sealed ones. However, a premise is crucial before showing some examples. When using any EM imaging technique, either TEM or SEM based, no living specimen could be directly looked at without destroying it. That is due to the intrinsic conditions needed for any electron microscope to work (high vacuum and radiation damage due to the electrons-matter interactions) that are incompatible with the high water content, low density, and very low hardness of any living organism. To look at any living matter *post mortem*, so far a very large series of experimental protocol have been then developed, which allow making it rigid, dehydrated or frozen, and possibly with enough contrast if seen by a transmission geometry. In any case, all preparation protocols unavoidably require to kill either the cells or the micro-organisms prior to inserting them in any EM. The *in situ* liquid sample holders are then the only devices that are currently able to allow looking at living matter without killing it, and keeping it into a physiological aqueous environment, even if some effects of the radiation damage have to be taken into account. First, the small temperature rise can alter diffusion and reaction rates via convective motions within the liquid volume. Second, nonthermal effects may be more critical and more complicated to deal with: (a) high-energy electrons in water give rise to the pretty long-lived species' production such as OH radicals and hydrated electrons, even if charged species could quench radicals resulting in the concomitant reduction of their reactivity in solution; (b) substrate chemistry also plays a nonnegligible role since reactive species can be generated from interactions between the beam and the substrate, i.e., the thin windows that seal the E-Cell; (c) organic specimens are known to be intensely affected by a small enough electron

dose, which means that for pristine biological materials, structural damage begins to happen at the subnanometer scale when the low electron dose of $\sim 10^2$ electrons per nm^2 is exceeded. This effect could be limited: (a) considering that the electron dose usually scales quadratically with the resolution, and then the latter could be appropriately chosen in order to have still good images but low radiation damage; (b) making use of an ultrasensitive CMOS camera, which allows to work using very low electron doses. If higher electron doses are required, the main way to preserve the cell/organism ultrastructure is stabilizing it by a chemical or cryofixation.
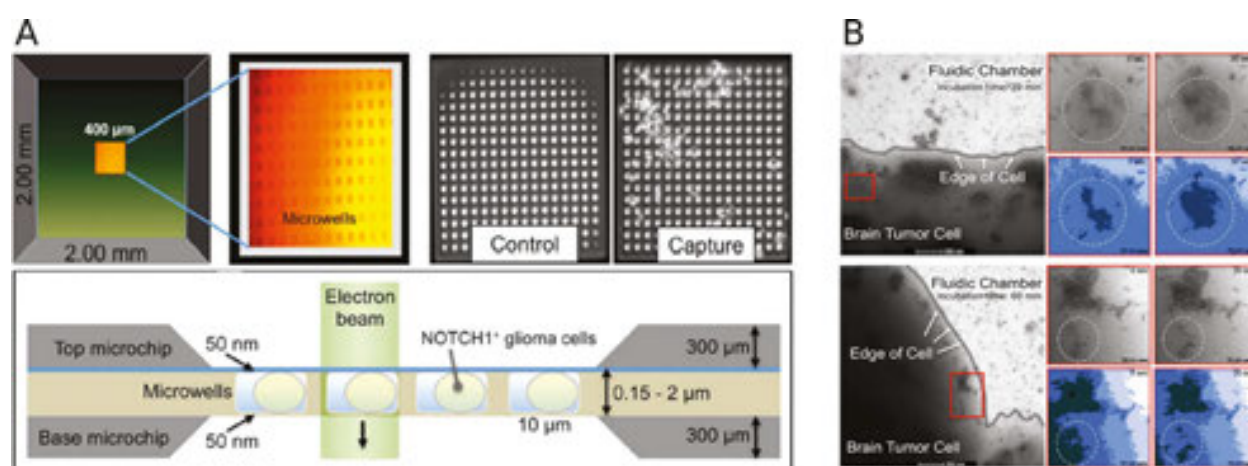

Figure 13. (A) Top image: single Si microchip with an electron-transparent SiN window. The sizes of the microchip are 2.0 × 2.3 × 0.3 117. Bottom image: sketch of a microfluidic chamber constituted by two Si microchips such as the ones presented in the top image and showing the liquid flow direction. Adapted with permission from [107, 108]. (B) Liquid STEM images of COS7 fibroblast cells labeled EGF-Au. Left image: edge of a fixed COS7 cell after 5 min incubation with EGF-Au. The labels are visible as bright spots and the cellular material is shown as light-gray matter on a dark-gray background (pixel size: 5.7 nm). Central image: COS7 cell incubated with EGF-Au for 10 min and then in buffer (without EGF-Au) for additional 15 min. Circular cluster of labeled EGF receptors are visible. Arrow 1 indicates sharp-edged gold labels in the cluster, whereas the labels in the cluster at arrow 2 appear blurred and cannot be distinguished as individual entities, indicating that cluster 2 is out of the vertical plane of focus. The observation of circular clusters of labels at different vertical positions in the cell indicates that the gold nanoparticles labels were internalized (pixel size: 5.7 nm). Right image: sample shown in left image, but imaged after the flow cell opening and sample drying in air. The dried sample displays much stronger contrast on the cellular material: the white large zones in the image correspond to the edge of a dried cell, while the gold nanoparticles labels are still visible as bright spots (pixel size: 8.9 nm). Adapted with permission from [107]. (C) Left image: COS7 cell edge labeled with EGF-Au, where the bright spots indicate the labels (pixel size: 2.9 nm). Central image: magnification of the area defined by the white square in left image showing the individual labels. Right top line profile: HAADF signal as a function of the electron probe position over an individual gold nanoparticle, corresponding to the line labeled "C" in the central image. Right bottom line profile: HAADF signal as detected on a 10 nm gold nanoparticle at the bottom of 1.3 μm thick liquid layer (10% PBS buffer in water) in a test sample without cells (pixel size was 0.91 nm). Adapted with permission from [107].

As first example of study of biological living matter by *in situ* E-Cell for liquid specimens, we report here what Liu et al. showed in their paper [115]. It reports the detailed fabrication using microelectromechanical system (MEMS) techniques to obtain a novel microchip constituted by two SiO$_2$ films used as a substrate and the 9 nm thin windows for *in situ* imaging of living organisms in aqueous environment using a conventional TEM geometry. Such a kind of microchips—with a gap between them ranging from 2 to 5 μm—allowed the effective TEM observation of living bacteria *Escherichia coli* and the tellurite reduction process in *Klebsiella pneumonia*, the height of which were estimated ranging between 0.5 and 1μm. The most important results of this paper were (a) the capability of bacterium *K. pneumoniae* and the yeast *Saccharomyces cerevisiae* to stay alive onto the microchip substrate under continuous electron beam irradiation needed for the TEM imaging for up to 14 and 42 s, respectively; (b) the possibility to follow over time, even if with not very high resolution as expected from Eq. (2), biological processes such as the tellurite reduction by *K. pneumonia*.

As already mentioned and shown by Eq. (3), the use of STEM allowed to achieve a dramatically increased resolution and to image by using HAADF geometry even very small heavy particles dispersed in a light liquid medium. This was the case of Au-labeled eukaryotic fibroblast cells (COS7) immersed in a several micrometer-thick liquid layer [107, 109]. In both the papers a flow liquid E-Cell was used, allowing the aqueous solution to pour through the E-Cell and around the whole fibroblast cells. The experimental configuration is reported in **Figure 13A**. The cells were grown, then labeled, and finally fixed prior to be inserted in the flow E-Cell, on the internal side of the silicon nitride film that was finally placed to seal the upper part of the E-Cell, in order to maximize the STEM resolution according to Eq. (3). The cells' immunolabeling was realized by using gold NPs sizing 10 nm, in order to target the epidermal growth factor (EGF) molecules bound to the cellular EGF receptors. Thus, using a water layer 10 μm thick, the theoretical resolution limit determined by using Eq. (3) was found to be equal to 1.9 nm. In agreement with that, the 10 nm sized labeling gold NPs were detected with a spatial resolution of about 4 nm, as shown in **Figure 13B** and **C**, using the STEM in HAADF geometries, and performed with a beam accelerated by a voltage of 200 kV and a dwell time of 20 μs. If it is not weird that the electron beam did not perturb the fixed cells, it is however remarkable that for the dose used (7 × 10^4 electrons per nm^2) and within the flowing liquid no visible damage consequences were observed on the spatial distribution of the labeling NPs on the cells.

As last and most recent example the results achieved by Pohlmann *et al.* are shown [110]. In their paper they showed an *in situ* TEM imaging, time resolved, of the uptake of typical drug delivery vehicles—in such a case gold nanorods (GNR) encapsulated in polyvinylpyridine (PVP)—from glioblastoma stem cells (GSCs), which actually is one of the most aggressive cancers among brain tumors. This kind of study is quite interesting, allowing to image by TEM the evolution over time of NP uptake from living cells, a phenomenon so far investigated just by light/confocal microscopy. To perform it, the authors first prepared a multiwell E-Cell with a maximum height of 2 μm where the GSCs were forced to be tethered on the lower side, thanks to a surface functionalization that involved their NOTCH1 receptors, as shown in **Figure 14A**. Then, the GSCs contained in the multiwell E-Cell were incubated together with the

PVP-GNR NRs for 20 and 60 min, respectively, prior to inserting the sealed E-Cell into the TEM. The evolution of the PVP-GNRs within the GSCs was then followed over a total time of 30 s, using the TEM classical geometry performed at medium magnification, and with a high contrast objective lens and an electron beam acceleration voltage of 120 kV. Even under these conditions, the resolution was enough to study the PVP-GNRs uptake evolution over time. As shown in **Figure 14B**, the movement of the PVP-GNRs inside the GSCs is similar for both the incubation times: a local displacement of the PVP-GNRs and the solution surrounding them were observed. The main difference between the GSCs incubated for 20 and 60 min with the PVP-GNRs consisted in the number of those uptaken from the GSCs: higher the incubation time, higher the amount of PVP-GNRs internalized from the tumor cells.

Figure 14. (A) First row, left images: sketches of microchip with integrated microwells (10 μm in diameter) functional-ized to specifically capture GS9-6/NOTCH+ glioblastoma stem cells; right images: comparison between the functional-ized microwells (called "capture") and the negative control, i.e., identical microwells not treated for functionalization and then not able to tether GSCs. Second row: sketch showing a cross-sectional view of the microfluidic system con-taining GSC positioned in the TEM column. Adapted with permission from [110]. (B) Gold nanorods penetrated in a GSCs after two different times of incubation. Top images show the capability of unlabeled gold nanorods to perforate the cells within 20 min incubation period; moreover, the liquid dispersed around the nanorods displaces their position within a common region. These movements are represented in a contour map generated at the same threshold level and within the same region of interest at the initial imaging stage (0 s) and final stage (30 s). Regions exhibiting the greatest density (included both nanorods and their surrounding liquid) were contoured at the darker colored thresh-old while regions showing less density were represented using increasingly lighter gradients of color. Bottom images: cell incubated for 60 min, where more NPs inside the cell than in the solution are observed, if compared to the sample incubated for 20 min. Adapted with permission from [110].

5. Conclusions

In this chapter, some of the most recent developments for the *in situ* TEM and STEM imaging techniques have been shown. The chapter aimed at showing the impact on the *in situ* TEM/ STEM imaging of the progress achieved in the last 10–15 years in terms of novel microscope architecture developments, fabrication and commercial availability of novel and much more performing dedicated specimen holders. This in turn has allowed achieving unprecedented

results in terms of sample stability and diversity of setups, variation of the local sample environment, and possible external *stimuli*. Due to the vastness of the topic, the three sections of this chapter have been dedicated to describe three particular applications of the *in situ* TEM/STEM that witness how this technique evolved in the last decade: the *in situ* sample heating under high vacuum condition, the *in situ* sample heating in a controlled gaseous atmosphere, and, finally, the *in situ* imaging of samples immersed in a liquid layer of user-controlled thickness. The importance of these improvements lies in the widening of their possible application not only to inorganic but also to biological materials, even in living conditions, which paves the way to novel, so far unattainable studies.

Author details

Alberto Casu, Elisa Sogne, Alessandro Genovese, Cristiano Di Benedetto, Sergio Lentijo Mozo, Efisio Zuddas, Francesca Pagliari and Andrea Falqui[*]

*Address all correspondence to: andrea.falqui@kaust.edu.sa

King Abdullah University of Science and Technology (KAUST), Biological and Environmental Sciences and Engineering (BESE) Division, Thuwal, Kingdom of Saudi Arabia

References

[1] Freitag B, Knippels G, Kujawa S, Van der Stam M, Hubert D, Tiemeijer PC, Kisielowski C, Denes P, Minor A, Dahmen U. First performance measurements and application results of a new high brightness Schottky field emitter for HR S/TEM at 80–300 kV acceleration voltage. Microsc. Microanal. 2008; 14:1370–1371. DOI: 10.1017/S1431927608087370.

[2] Haider M, Uhlemann S, Schwan E, Rose H, Kabius B, Urban K. Electron microscopy image enhanced. Nature 1998; 392:768–769. DOI: 10.1038/33823.

[3] Krivanek OL, Dellby N, Lupini AR. Towards sub Angstrom electron beams. Ultramicroscopy. 1999; 78:1–11. DOI: 10.1016/S0304 3991(99)00013 3.

[4] Tiemeijer PC, Van Lin JHA, De Long AF. First results of a monochromatized 200 kV TEM. Microsc. Microanal. 2001; 7:234–235.

[5] Kasper E. Field electron emission systems. In: Barer R, Cosslett VE, editors. Advances in Optical and Electron Microscopy. Vol. 8. Academic, London. p. 207; 1982.

[6] Von Harrach HS, Dona P, Freitag B, Soltau H, Niculae A, Rohde M. An integrated multiple silicon drift detector system for transmission electron microscopes. J. Phys. Conf. Ser. 2010; 241:012015. DOI: 10.1088/1742 6596/241/1/012015.

[7] Gubbens A, Barfels M, Trevor C, Twesten R, Mooney P, Thomas P, Menon N, Kraus B, Mao C, McGinn B. The GIF quantum, a next generation post column imaging energy filter. Ultramicroscopy 2010; 110:962–970. DOI: 10.1016/j.ultramic.2010.01.009.

[8] Ruskina RS, Yub Z, Grigorieff N. Quantitative characterization of electron detectors for transmission electron microscopy. J. Struct. Biol. 2013; 184:385–393. DOI: 10.1016/j.jsb. 2013.10.016.

[9] Heinemann K, Poppa H. Direct observation of small cluster mobility and ripening. Thin Solid Films. 1976; 33:237–251. DOI: 10.1016/0040 6090(76)90084 5.

[10] Ruault MO, Chaumont J, Bernas H. Transmission electron microscopy study of ion implantation induced Si amorphization. Nucl. Instrum. Methods Phys. Res. 1983; 209:351–356. DOI: 10.1016/0167 5087(83)90822 0.

[11] Chen SH, Zheng LR, Carter CB, Mayer JW. Transmission electron microscopy studies on the lateral growth of nickel silicides. J. Appl. Phys. 1985; 57:258–263. DOI: 10.1063/1.335482.

[12] Dannenberg R, Stach E, Groza JR, Dresser BJ. TEM annealing study of normal grain growth in silver thin films. Thin Solid Films. 2000; 379:133–138. DOI: 10.1016/S0040 6090(00)01570 4.

[13] Kamino T, Saka H. A newly developed high resolution hot stage and its application to materials characterization. Microsc. Microanal. Microstruct. 1993; 4:127–135. DOI: 10.1051/mmm:0199300402 3012700.

[14] Zhang M, Olson EA, Twesten RD, Wen JG, Allen LH, Robertson IM, Petrov I. In situ transmission electron microscopy studies enabled by microelectromechanical system technology. J. Mater. Res. 2005; 20:1802–1807. DOI: 10.1557/JMR.2005.0225.

[15] Allard LF, Bigelow WC, Jose Yacaman M, Nackashi DP, Damiano J, Mick SE. A new MEMS based system for ultra high resolution imaging at elevated temperatures. Microsc. Res. Tech. 2009; 72:208–215. DOI: 10.1002/jemt.20673.

[16] Sperling RA, Rivera Gil P, Zhang F, Zanella M, Parak WJ. Biological applications of gold nanoparticles. Chem. Soc. Rev. 2008; 37:1896–1908. DOI: 10.1039/b712170a.

[17] DeLong RK, Reynolds CM, Malcolm Y, Schaeffer A, Severs T, Wanekaya A. Functionalized gold nanoparticles for the binding, stabilization, and delivery of therapeutic DNA, RNA, and other biological macromolecules. Nanotechnol. Sci. Appl. 2010; 3:53–63. DOI: 10.2147/NSA.S8984.

[18] Zhou ZY, Tian N, Li JT, Broadwell I, Sun SG. Nanomaterials of high surface energy with exceptional properties in catalysis and energy storage. Chem. Soc. Rev. 2011; 40:4167–4185. DOI: 10.1039/c0cs00176g.

[19] Li N, Zhao P, Astruc D. Anisotropic gold nanoparticles: synthesis, properties, applications, and toxicity. Angew. Chem. Int. Ed. 2014; 53:1756–1789. DOI: 10.1002/anie.201300441.

[20] Langille MR, Personick ML, Zhang J, Mirkin CA. Defining rules for the shape evolution of gold nanoparticles. J. Am. Chem. Soc. 2012; 134:14542–14554. DOI: 10.1021/ja305245g.

[21] Koga K, Ikeshoji T, Sugawara KI. Size and temperature dependent structural transitions in gold nanoparticles. Phys. Rev. Lett. 2004; 92:115507. DOI: 10.1103/PhysRevLett.92.115507.

[22] Kuo CL, Clancy P. Melting and freezing characteristics and structural properties of supported and unsupported gold nanoclusters. J. Phys. Chem. B. 2005; 109:13743–13754. DOI: 10.1021/jp0518862.

[23] Barnard AS, Young NP, Kirkland AI, van Huis MA, Xu H. Nanogold: a quantitative phase map. ACS Nano. 2009; 3:1431–1436. DOI: 10.1021/nn900220k.

[24] Young NP, van Huis MA, Zandbergen HW, Xu H, Kirkland AI. Transformations of gold nanoparticles investigated using variable temperature high resolution transmission electron microscopy. Ultramicroscopy. 2010; 110:506–516. DOI: 10.1016/j.ultramic.2009.12.010.

[25] Baumgardner WJ, Yu Y, Hovden R, Honrao S, Hennig RG, Abruna HD, Muller D. Nanoparticle metamorphosis: an in situ high temperature transmission electron microscopy study of the structural evolution of heterogeneous Au:Fe2O3 nanoparticles. ACS Nano. 2014; 8:5315–5322. DOI: 10.1021/nn501543d.

[26] Figuerola A, van Huis M, Zanella, M, Genovese A, Marras S, Falqui A, Zandbergen HW, Cingolani R, Manna L. Epitaxial CdSe Au nanocrystal heterostructures by thermal annealing. Nano Lett. 2010; 10:3028–3036. DOI: 10.1021/nl101482q.

[27] Lavieville R, Zhang Y, Casu A, Genovese A, Manna L, Di Frabrizio E, Krahne R. Charge transport in nanoscale "all inorganic" networks of semiconductor nanorods linked by metal domains. ACS Nano. 2012; 6:2940–2947. DOI: 10.1021/nn3006625.

[28] Liu Z, Che R, Elzatahry AA, Zhao D. Direct imaging Au nanoparticle migration inside mesoporous silica channels. ACS Nano. 2014; 8:10455–10460. DOI: 10.1021/nn503794v.

[29] Costi R, Saunders AE, Banin U. Colloidal hybrid nanostructures: a new type of functional materials. Angew. Chem. Int. Ed. 2010; 49:4878–4897. DOI: 10.1002/anie.200906010.

[30] Jun YW, Choi JS, Cheon J. Shape Control of Semiconductor and Metal Oxide Nanocrystals through Nonhydrolytic Colloidal Routes. Angew. Chem. Int. Ed. 2006; 45:3414–3439. DOI: 10.1002/anie.200503821.

[31] Zheng H, Smith RK, Jun YW, Kisielowski C, Dahmen U, Alivisatos AP. Observation of single colloidal platinum nanocrystal growth trajectories. Science. 2009; 324:1309–1312. DOI: 10.1126/science.1172104.

[32] Asoro MA, Desiderio K, Ferreira PJ. In situ transmission electron microscopy observations of sublimation in silver nanoparticles. ACS Nano. 2013; 7:7844–7852. DOI: 10.1021/nn402771j.

[33] Li H, Zanella M, Genovese A, Povia M, Falqui A, Giannini C, Manna L. Sequential cation exchange in nanocrystals: preservation of crystal phase and formation of metastable phases. Nano Lett. 2011; 11:4964–4970. DOI: 10.1021/nl202927a.

[34] Hellebusch DJ, Manthiram K, Beberwyck BJ, Alivisatos AP. In situ transmission electron microscopy of cadmium selenide nanorod sublimation. J. Phys. Chem. Lett. 2015; 6:605–611. DOI: 10.1021/jz502566m.

[35] Hudak BM, Chang YJ, Yu L, Li G, Edwards DN, Guiton BS. Real time observation of the solid liquid vapor dissolution of individual tin(IV) oxide nanowires. ACS Nano. 2014; 8:5441–5448. DOI: 10.1021/nn5007804.

[36] Yalcin AO, Fan Z, Goris B, Li WF, Koster RS, Fang CM, Van Blaaderen A, Casavola M, Tichelaar FD, Bals S, Van Tendeloo G, Vlugt TJH, Vanmaekelbergh D, Zandbergen HW, Van Huis MA. Atomic resolution monitoring of cation exchange in CdSe PbSe hetero-nanocrystals during epitaxial solid–solid–vapor growth. Nano Lett. 2014; 14:3661–3667. DOI: 10.1021/nl501441w.

[37] De Trizio L, De Donato F, Casu A, Genovese A, Falqui A, Povia M, Liberato M. Colloidal CdSe/Cu^{3}P/CdSe and their evolution upon thermal annealing. ACS Nano. 2013; 7:3997–4005. DOI: 10.1021/nn3060219.

[38] Geim AK, Novoselov KS. The rise of graphene. Nat. Mater. 2007; 6: 183–191. DOI: 10.1038/nmat1849.

[39] Balandin AA, Ghosh S, Bao W, Calizo I, Teweldebrhan D, Miao F, Lau CN. Superior thermal conductivity of single layer graphene. Nano Lett. 2008; 8:902–907. DOI:10.1021/nl0731872.

[40] Soldano C, Mahmood A, Dujardin E. Production, properties and potential of graphene. Carbon. 2010; 48:2127–2150. DOI: 10.1016/j.carbon.2010.01.058.

[41] Novoselov KS, Geim AK, Morozov SV, Jiang D, Zhang Y, Dubonos SV, Grigorieva IV, Firsov AA. Electric Field Effect in Atomically Thin Carbon Films. Science. 2004; 306:666–669. DOI: 10.1126/science.1102896.

[42] Reina A, Jia X, Ho J, Nezich D, Son H, Bulovic V, Dresselhaus MS, Kong J. Large area, few layer graphene films on arbitrary substrates by chemical vapor deposition. Nano Lett. 2009; 9:30–35. DOI: 10.1021/nl801827v.

[43] Yannopoulos SN, Siokou A, Nasikas NK, Dracopoulos V, Ravani F, Papatheodorou GN. CO2-laser-induced growth of epitaxial graphene on 6H-SiC (0001). Adv. Funct. Mater. 2012; 2:113–120. DOI: 10.1002/adfm.201101413.

[44] Park J, Mitchel WC, Grazulis L, Smith HE, Eyink KG, Boeckl JJ, Tomich DH, Pacley SD, Hoelscher JE. Epitaxial graphene growth by carbon molecular beam epitaxy (CMBE). Adv. Mater. 2010; 22:4140–4145. DOI: 10.1002/adma.201000756.

[45] Liu Z, Lin YC, Lu CC, Yeh CH, Chiu PW, Iijima S, Suenaga K. In situ observation of step edge in plane growth of graphene in a STEM. Nat. Commun. 2014; 5:4055. DOI: 10.1038/ncomms5055.

[46] Kotakoski J, Santos Cottin D, Krasheninnikov AV. Stability of graphene edges under electron beam: equilibrium energetics versus dynamic effects. ACS Nano. 2011; 6:671–676. DOI: 10.1021/nn204148h.

[47] He Z, He K, Robertson AW, Kirkland AI, Kim D, Ihm J, Yoon E, Lee GD, Warner JH. Atomic structure and dynamics of metal dopant pairs in graphene. Nano Lett. 2014; 14:3766–3772. DOI: 10.1021/nl500682j.

[48] Pi K, McCreary KM, Bao W, Han W, Chiang YF, Li Y, Tsai SW, Lau CN, Kawakami RK. Electronic doping and scattering by transition metals on graphene. Phys. Rev. B. 2009; 80:075406. DOI: 10.1103/PhysRevB.80.075406.

[49] Kano E, Hashimoto A, Kaneko T, Tajima N, Ohno T, Takeguchi M. Interactions between C and Cu atoms in single layer graphene: direct observation and modelling. Nanoscale. 2016; 8:529–535. DOI: 10.1039/C5NR05913E.

[50] Ma J, Alfe D, Michaelides A, Wang E. Stone Wales defects in graphene and other planar sp2 bonded materials. Phys. Rev. B. 2009; 80:033407. DOI: 10.1103/PhysRevB.80.033407.

[51] Ramasse QM, Zan R, Bangert U, Boukhvalov DW, Son YW, Novoselov, KS. Direct experimental evidence of metal mediated etching of suspended graphene. ACS Nano. 2012; 6:4063–4071. DOI: 10.1021/nn300452y.

[52] Kim MJ, Wanunu M, Bell DC, Meller A. Rapid fabrication of uniformly sized nanopores and nanopore arrays for parallel DNA analysis. Adv. Mater. 2006; 18:3149–3153. DOI: 10.1002/adma.200601191.

[53] Liu K, Feng J, Kis A, Radenovic A. Atomically thin molybdenum disulfide nanopores with high sensitivity for DNA translocation. ACS Nano. 2014; 8:2504–2511. DOI: 10.1021/nn406102h.

[54] Xu T, Xie X, Yin K, Sun J, He L, Sun L. Controllable atomic-scale sculpting and deposition of carbon nanostructures on graphene. Small. 2014; 10:1724–1728. DOI: 10.1002/smll.201303377.

[55] He K, Robertson AW, Gong C, Allen CS, Xu Q, Zandbergen H, et al. Controlled formation of closed edge nanopores in graphene. Nanoscale. 2015; 7:11602–11610. DOI: 10.1039/C5NR02277K.

[56] Asoro MA, Kovar D, Ferreira PJ. Effect of surface carbon coating on sintering of silver nanoparticles: in situ TEM observations. Chem. Commun. 2014; 50:4835–4838. DOI: 10.1039/c4cc01547a.

[57] Chen C, Hu Z, Li Y, Liu L, Mori H, Wang Z. In Situ high resolution transmission electron microscopy investigation of overheating of Cu nanoparticles. Sci. Rep. 2016; 6:19545. DOI: 10.1038/srep19545.

[58] Romankov S, Park YC. In situ high temperature TEM observation of material escape from a surface of CoFeNi/Cu/ZrAlO composite into the amorphous carbon layer. J. Alloys Compd. 2015; 632:408–416. DOI: 10.1016/j.jallcom.2015.01.214.

[59] Tang DM, Liu C, Yu WJ, Zhang LL, Hou PX, Li JC, Li F, Bando Y, Golberg D, Cheng HM. Structural changes in iron oxide and gold catalysts during nucleation of carbon nanotubes studied by in situ transmission electron microscopy. ACS Nano. 2014; 8:292–301. DOI: 10.1021/nn403927y.

[60] Boston R, Schnepp Z, Nemoto Y, Sakka Y, Hall SR. In situ TEM observation of a microcrucible mechanism of nanowire growth. Science. 2014; 344:623–626. DOI: 10.1126/science.1251594.

[61] Casu A, Genovese A, Manna L, Longo P, Buha J, Botton GA, Lazar S, Kahaly MU, Schwingenschloegl U, Prato M, Li H, Ghosh S, Palazon F, De Donato F, Lentijo Mozo S, Zuddas E, Falqui A. Cu2Se and Cu nanocrystals as local sources of copper in thermally activated in situ cation exchange. ACS Nano. 2016; 10:2406–2414. DOI: 10.1021/acsnano.5b07219.

[62] Marton L. Marton L. Electron microscopy of biological objects (La microscopie electronique des objets biologiques). Bull. Classe. Sci. Acad. Roy Belgique. 1935; 21:553–564

[63] Hashimoto H, Naiki T, Eto T, Fujiwara K. High temperature gas reaction specimen chamber for an electron microscope. Jpn. J. Appl. Phys. 1968; 7:946–952. DOI: 10.1143/JJAP.7.946.

[64] Parsons DF. Structure of wet specimens in electron microscopy. Science. 1974; 186:407–414. DOI: 10.1126/science.186.4162.407.

[65] Mehraeen S, McKeown JT, Deshmukh PV, Evans JE, Abellan P, Xu P, Reed BW, Taheri ML, Fischione PE, Browning ND. A (S)TEM gas cell holder with localized laser heating for in situ experiments. Microsc. Microanal. 2013; 19:470–478. DOI: 10.1017/S1431927612014419.

[66] Turner JN, See CW, Ratkowski AJ, Chang BB, Parsons DF. Design and operation of a differentially pumped environmental chamber for the HVEM. Ultramicroscopy. 1981; 6:267–280. DOI: 10.1016/s0304 3991(81)80162 3.

[67] Lee TC, Dewald DK, Eades JA, Robertson IM, Birnbaum HK. An environmental cell transmission electron microscope. Rev. Sci. Instrum. 1991; 62:1438–1444. DOI: 10.1063/1.1142464.

[68] Boyes ED, Gai PL. Environmental high resolution electron microscopy and applications to chemical science. Ultramicroscopy. 1997; 67:219–232. DOI: 10.1016/S0304 3991(96)00099 X.

[69] Sharma R. Design and applications of environmental cell transmission electron microscope for in situ observations of gas–solid reactions. Microsc. Microanal. 2001; 7:494–506. DOI: 10.1007/s10005 001 0015 1.

[70] Hansen TW, Wagner JB. Environmental transmission electron microscopy in an aberration corrected environment. Microsc. Microanal. 2012; 18:684–690. DOI: 10.1017/S1431927612000293.

[71] Boyes ED, Gai PL. Visualising reacting single atoms under controlled conditions: advances in atomic resolution in situ environmental (scanning) transmission electron microscopy (E(S)TEM). C. R. Physique 2014; 15:200–213. DOI: 10.1016/j.crhy.2014.01.002.

[72] Kawasaki T, Ueda K, Ichihashi M, Tanji T. Improvement of windowed type environmental cell transmission electron microscope for in situ observation of gas solid interactions. Rev. Sci. Instrum. 2009; 80:113701. DOI: 10.1063/1.3250862.

[73] Baker RTK, Barber MA, Harris PS, Feates FS, Waite RJ. Nucleation and growth of carbon deposits from the nickel catalyzed decomposition of acetylene. J. Catal. 1972; 26:51–62. DOI: 10.1016/0021 9517(72)90032 2.

[74] Baker RTK, Harris PS. Controlled atmosphere electron microscopy. J. Phys. E. 1972; 5:793–797. DOI: 10.1088/0022 3735/5/8/024.

[75] Parkinson GM. High resolution, in situ controlled atmosphere transmission electron microscopy (CATEM) of heterogeneous catalysts. Catal. Lett. 1989; 2:303–307. DOI: 10.1007/BF00770228.

[76] Giorgio S, Joao SS, Nitsche S, Chaudanson D, Sitja G, Henry CR. Environmental electron microscopy (E TEM) for catalysts with a closed E cell with carbon windows. Ultramicroscopy. 2006; 106:503–507. DOI: 10.1016/j.ultramic.2006.01.006.

[77] de Jonge N, Bigelow WC, Veith GM. Atmospheric pressure scanning transmission electron microscopy. Nano Lett. 2010; 10:1028–1031. DOI: 10.1021/nl904254g.

[78] Petkov N. In situ real time TEM reveals growth, transformation and function in one dimensional nanoscale materials: from a nanotechnology perspective. ISRN Nanotechnology. 2013; 2013:893060. DOI: 10.1155/2013/893060.

[79] Hansen TW, Wagner JB. Controlled Atmosphere Transmission Electron Microscopy. Springer International Publishing; Switzerland, 2016. 329 pp. DOI: 10.1007/978 3 319 22988 1.

[80] Suzuki M, Yaguchi T, Zhang XF. High resolution environmental transmission electron microscopy: modeling and experimental verification. Microscopy. 2013; 62:437–450. DOI: 10.1093/jmicro/dft001.

[81] Wagner JB, Cavalca F, Damsgaard CD, Duchstein LDL, Hansen TW. Exploring the environmental transmission electron microscope. Micron. 2012; 43:1169–1175. DOI: 10.1016/j.micron.2012.02.008.

[82] Xin HL, Niu K, Alsem DH, Zheng H. In situ TEM study of catalytic nanoparticle reactions in atmospheric pressure gas environment. Microscopy Microanal. 2013; 19:1558–1568. DOI: 10.1017/S1431927613013433.

[83] Zhang XF, Kamino T. Imaging gas–solid interactions in an atomic resolution environmental TEM. Micros. Today. 2006; 14:16–18.

[84] Bright AN, Yoshida K, Tanaka N. Influence of total beam current on HRTEM image resolution in differentially pumped E TEM with nitrogen gas. Ultramicroscopy. 2013; 124:46–51. DOI: 10.1016/j.ultramic.2012.08.007.

[85] Takeda S, Kuwauchi Y, Yoshida H. Environmental transmission electron microscopy for catalyst materials using a spherical aberration corrector. Ultramicroscopy. 2015; 151:178–190. DOI:10.1016/j.ultramic.2014.11.017.

[86] Jinschek JR, Helveg S. Image resolution and sensitivity in an environmental transmission electron microscope. Micron. 2012; 43:1156–1168. DOI: 10.1016/j.micron. 2012.01.006.

[87] Cavalca F, Laursen, AB, Wagner JB, Damsgaard CD, ChorkendorffIb, Hansen TW. Light induced reduction of cuprous oxide in an environmental transmission electron microscope. Chem. Cat. Chem. 2013; 5:2667–2672. DOI: 10.1002/cctc.201200887.

[88] Jeangros Q, Hansen TW, Wagner JB, Dunin Borkowski RE, Hébert C, Van herle J, Hessler Wyser A. Oxidation mechanism of nickel particles studied in an environmental transmission electron microscope. Acta Mater. 2014; 67:362–372. DOI: 10.1016/j.acta-mat.2013.12.035.

[89] Xin HL, Pach EA, Diaz RE, Stach EA, Salmeron M, Zheng H. Revealing correlation of valence state with nanoporousstructure in cobalt catalyst nanoparticles by in situ environmental TEM. ACS Nano. 2012; 6:4241–4247. DOI: 10.1021/nn3007652.

[90] Serve A, Epicier T, Aouine M, Cadete Santos Aires FJ, Obeid E, Tsampas M, Pajot K, Vernoux P. Investigations of soot combustion on yttria stabilized zirconia by environ-

mental transmission electron microscopy (E TEM). Appl. Catal. A Gen. 2015; 504:74–80. DOI: 10.1016/j.apcata.2015.02.030.

[91] Chenna S, Crozier PA. Operando transmission electron microscopy: a technique for detection of catalysis using electron energy loss spectroscopy in the transmission electron microscope. ACS Catal. 2012; 2:2395–2402. DOI: 10.1021/cs3004853.

[92] Creemer JF, Helveg S, Hoveling GH, Ullmann S, Molenbroek AM, Sarro PM, Zandbergen HW. Atomic scale electron microscopy at ambient pressure. Ultramicroscopy. 2008; 108:993–998. DOI: 10.1016/j.ultramic.2008.04.014.

[93] Allard LF, Overbury SH, Bigelow WC, Katz MB, Nackashi DP, Damiano J. Novel MEMS based gas cell/heating specimen holder provides advances imaging capabilities for in situ reaction studies. Microsc. Microanal. 2012; 18:656–666. DOI: 10.1017/S1431927612001249.

[94] Yokosawa T, Alan T, Pandraud G, Dam B, Zandbergen H. In situ TEM on (de)hydrogenation of Pd at 0.5–4.5 bar hydrogen pressure and 20–400°C. Ultramicroscopy. 2012; 112:47–52. DOI: 10.1016/j.ultramic.2011.10.010.

[95] Doll T, Hochberg M, Barsic D, Scherer A. Micro machined electron transparent alumina vacuum windows. Sens. Actuat. A Phys. 2000; 87:52–59. DOI: 10.1016/S0924 4247(00)00461 1.

[96] Wu F, Yao N. Advances in windowed gas cells for in situ TEM studies. Nano Energy 2015; 13:735–756. DOI: 10.1016/j.nanoen.2015.03.015.

[97] Vendelbo SB, Elkjær CF, Falsig H, Puspitasari I, Dona P, Mele L, Morana B, Nelissen BJ, van Rijn R, Creemer JF, Kooyman PJ, Helveg S. Visualization of oscillatory behaviour of Pt nanoparticles catalysing CO oxidation. Nat. Mater. 2014; 13:884–890. DOI: 10.1038/nmat4033.

[98] Creemer JF, Helveg S, Kooyman PJ, Molenbroek AM, Zandbergen HW, Sarro PM. A MEMS reactor for atomic scale microscopy of nanomaterials under industrially relevant conditions. J. Microelectromech. Syst. 2010; 19:254–264. DOI: 10.1109/JMEMS.2010.2041190.

[99] Yaguchi T, Suzuki M, Watabe A, Nagakubo Y, Ueda K, Kamino T. Development of a high temperature–atmospheric pressure environmental cell for high resolution TEM. J. Electr. Microsc. 2011; 6:217–225. DOI: 10.1093/jmicro/dfr011.

[100] Sun L, Wook Noh K, Wen JG, Dillon SJ. In situ transmission electron microscopy observation of silver oxidation in ionized/atomic gas. Langmuir 2011; 27:14201–14206. DOI: 10.1021/la202949c.

[101] Zhang S, Chen C, Cargnello M, Fornasiero P, Gorte RJ, Graham GW, Pan X. Dynamic structural evolution of supported palladium ceria core shell catalysts revealed by in situ electron microscopy. Nat. Commun. 2015; 6. DOI: 10.1038/ncomms8778.

[102] Hell SW. Far field optical nanoscopy. Science. 2007; 316(5828):1153–1158. DOI:10.1126/science.1137395.

[103] Abrams IM, McBain JW. A closed cell for electron microscopy. Science. 1944; 100(2595): 273–274. DOI: 10.1126/science.100.2595.273.

[104] Abrams IM, McBain JW. A closed cell for electron microscopy. Appl. Phys. 1944; 15:607–609. DOI: 10.1063/1.1707475.

[105] Fullam EF. A closed wet cell for the Electron Microscope. Rev. Sci. Instrum. 1972; 43:245–247. DOI: 10.1063/1.1685603.

[106] Gai PL. Development of wet environmental TEM (wet E TEM) for in situ studies of liquid catalyst reactions on the nanoscale. Microsc. Microanal. 2002; 8:21–28.

[107] de Jonge N, Peckys DB, Kremers GJ, Piston DW. Electron microscopy of whole cells in liquid with nanometer resolution. PNAS. 2009; 106:2159–2164. DOI: 10.1073/pnas.0809567106.

[108] de Jonge N, Ross FM. Electron microscopy of specimens in liquid. Nat. Nanotech. 2011; 6:695–704. DOI: 10.1038/nnano.2011.161.

[109] Dukes M, Peckys DB, de Jonge N. Correlative fluorescence microscopy and scanning transmission electron microscopy of quantum dot labeled proteins in whole cells in liquid. ACS Nano. 2010; 4(7):4110–4116. DOI: 10.1021/nn1010232.

[110] Pohlmann ES, Patel K, Guo S, Dukes MJ, Sheng Z, Kelly DF. Real time visualization of nanoparticles interacting with glioblastoma stem cells. Nano Lett. 2015; 15:2329–2335. DOI: 10.1021/nl504481k.

[111] Williamson MJ, Tromp RM, Vereecken PM, Hull R, Ross FM. Dynamic microscopy of nanoscale cluster growth at the solid–liquid interface. Nat. Mater. 2003; 2:532–536. DOI: 10.1038/nmat944.

[112] Radisic A, Vereecken PM, Hannon JB, Searson PC, Ross FM. Quantifying electrochemical nucleation and growth of nanoscale clusters using real time kinetic data. Nano Lett. 2006; 6:238–242. DOI: 10.1021/nl052175i.

[113] Zheng H, Smith RK, Jun Y, Kisielowski C, Dahmen U, Alivisatos AP. Observation of single colloidal platinum nanocrystal growth trajectories. Science. 2009; 324:1309–1312. DOI: 10.1126/science.1172104.

[114] Evans JE, Jungjohann KL, Browning ND, Arslan I. Controlled growth of nanoparticles from solution with in situ liquid transmission electron microscopy. Nano Lett. 2011; 11:2809–2813. DOI: 10.1021/nl201166k.

[115] Liu KL, Wu CC, Huang YJ, Peng HL, Chang HY, Chang P, Hsu L, Yew TR. Novel microchip for in situ TEM imaging of living organisms and bio reactions in aqueous conditions. Lab. Chip. 2008; 8:1915–1921. DOI: 10.1039/B804986F.

[116] Kim TH, Bae JH, Lee JW, Shin K, Lee JH, Kim MY, Yang CW. Temperature calibration of a specimen heating holder for transmission electron microscopy. Appl. Microsc. 2015; 45:95–100. DOI: 10.9729/AM.2015.45.2.95.

[117] Tanigaki T, Ito K, Nagakubo Y, Asakawa T, Kanemura T. An in situ heating TEM analysis method for an interface reaction. J. Electron Microsc. (Tokyo). 2009; 58:281–287. DOI: 10.1093/jmicro/dfp020.